THE ASTROPHYSICAL JOURNAL, 518:480–499, 1999 June 10

CALCULATION OF SOLAR IRRADIANCES. I. SYNTHESIS OF THE SOLAR SPECTRUM

JUAN FONTENLA,[1] ORAN R. WHITE, AND PETER A. FOX
High Altitude Observatory, National Center for Atmospheric Research,[2] P.O. Box 3000, Boulder, CO 80307
AND
EUGENE H. AVRETT AND ROBERT L. KURUCZ
Harvard-Smithsonian Center for Astrophysics, 60 Garden Street, Cambridge, MA 02138
Received 1998 June 25; accepted 1998 December 18

ABSTRACT

Variations in the total radiative output of the Sun as well as the detailed spectral irradiance are of interest to terrestrial and solar-stellar atmosphere studies. Recent observations provide measurements of spectral irradiance variations at wavelengths in the range 1100–8650 Å with improved accuracy, and correlative studies give procedures for estimating the spectral irradiance changes from solar activity records using indicators such as those derived from Ca II K and Mg II indices. Here we describe our approach to physical modeling of irradiance variations using seven semiempirical models to represent sunspots, plage, network, and quiet atmosphere. This paper gives methods and details, and some preliminary results of our synthesis of the variations of the entire irradiance spectrum. Our calculation uses object-oriented programming techniques that are very efficient and flexible. We compute at high spectral resolution the intensity as a function of wavelength and position on the disk for each of the structure types corresponding to our models. These calculations include three different approximations for the line source function: one suited for the very strong resonance lines where partial redistribution (PRD) is important, another for the most important nonresonance lines, and another approximation for the many narrow lines that are provided in Kurucz's listings. The image analysis and calculations of the irradiance variation as a function of time will be described in a later paper. This work provides an understanding of the sources of variability arising from solar-activity surface structures. We compute the Lyα irradiance to within 3% of the observed values. The difference between our computations and the Neckel & Labs data is 3% or less in the near-IR wavelengths at 8650 Å, and less than 1% in the red at 6080 Å. Near 4100 Å we overestimate the irradiance by 9%–19% because of opacity sources missing in our calculations. We also compute a solar cycle variability of 49% in the Lyα irradiance, which is very close to observed values. At wavelengths between 4100 Å and 1.6 μm, we obtain spectral irradiance variations ranging from −0.06% to 0.46% in the visible—the higher values correspond to the presence of strong lines. The variability in the IR between 1.3 and 2.2 μm is ∼ −0.15%.

Subject headings: Sun: atmosphere — Sun: general — Sun: infrared — Sun: UV radiation

1. INTRODUCTION

Measurements of total solar irradiance variability with solar activity over the 11 yr solar sunspot cycle were carried by the Earth Radiation Budget Experiment (ERBE) instrument on *Nimbus 7* (Hickey et al. 1988) and the Active Cavity Radiometer Irradiance Monitor (ACRIM) instrument on the *Solar Maximum Mission* (*SMM*; Willson 1982). These data give the first reliable insight on the variation of the solar radiative input to the Earth's atmosphere. At the same time, UV spectrometers on *Nimbus 7* and the *Solar Mesosphere Explorer* measured the variability in the wavelength range from 120 to 400 nm, a spectral region that is most important for ozone chemistry of the upper atmosphere. Correlative studies such as Tobiska (1992) relate irradiance at one wavelength to that at other wavelengths as well as to solar activity indices. These studies give statistical algorithms for estimating irradiances at times and wavelengths when no measurements are available. However, knowledge of how the solar spectrum originates, together with semiempirical models of specific solar structures observed on the disk, will improve our physical understanding of both the wavelength and temporal variability of the Sun's radiative output.

In response to the need for both measurement and interpretation of irradiance variations, the solar-terrestrial community and National Science Foundation started the program called Radiative Inputs from Sun to Earth (RISE) in 1991. Its mission is to measure and understand the origins of solar radiative variability. The program includes observational as well as analytical and theoretical components. Our study of the synthesis of the solar spectrum, sponsored by the RISE program, addresses the calculation of the amount of energy radiated by different structures on the visible solar surface and how they combine to produce the observed irradiances. The solar luminosity is about 3.86×10^{26} W, but in this paper we are interested only in the radiative energy flux at the Earth (or total solar irradiance), which is approximately 1368 W m^{-2} (Neckel & Labs 1984). The variability in this total solar irradiance over one solar activity cycle is observed as ∼0.2% (Willson & Hudson 1991).

Spectrum synthesis gives insight on the reliability of the use of surrogates to estimate total and spectral irradiances in the absence of direct measurement. This exploitation of the natural redundancy and coherence of the solar spectrum

[1] Present address: 771 West Dahlia, Louisville, CO 80027; jfontenla@mho.net.

[2] The National Center for Atmospheric Research is sponsored by the National Science Foundation.

can lead to more efficient measurement and analysis programs. Currently, the scaling formulae used to estimate the irradiances are obtained empirically from regression analyses of limited irradiance time series. Results from our study will give a physical understanding of the accuracy of empirical scaling rules and improve their application by determining how the various bands are physically related.

Our current work focuses on the following:

1. understanding the physical origins of the solar radiative variability arising from variations of surface structures through the solar activity cycle;
2. utilizing semiempirical models of the solar atmosphere to synthesize the intensity spectrum from features on the solar surface and, where discrepancies with observations are discovered, refining these models;
3. determining the distribution and evolution of surface features that contribute to irradiance variations;
4. combining the foregoing information with spectral synthesis models of lines and broad spectral bands to compute spectral and total irradiances for a particular state of the Sun;
5. determining those measurements that take best advantage of the basic redundancy in the solar spectrum so that irradiances at any wavelength can be inferred from available observations.

Computer programs for computing synthetic stellar spectra and opacity databases have been under development since 1965 at the Smithsonian Astrophysical Observatory (SAO) and are described by Kurucz & Furenlid (1980) and Kurucz & Avrett (1981). Kurucz (1992a, 1992b, 1992c) summarizes progress in accounting for opacity sources in the solar atmosphere and in constructing line lists of atomic and diatomic molecular transitions needed in synthesis calculations. The current state of the SAO synthesis program is given in a series of conference proceedings (Kurucz 1995). We use line and atomic data from the SAO program in our development of a new code that allows inclusion of new models of structures seen on the solar disk and line source functions computed with various methods to account for departures from thermodynamic equilibrium.

Our work recognizes the need to study the emergent radiation estimated from models such as the FAL series (Fontenla, Avrett, & Loeser 1989, 1992, 1993, hereafter FAL1, FAL2, and FAL3, respectively, and later work) and the need to improve our knowledge of the energy transport needed to interpret the relevant observations in the solar atmosphere. The present paper shows the basic approach used for our computations of the solar emergent intensity and spectral irradiance and defines the solar atmosphere models that we use for the calculations. These models are designed to represent the various types of structures observed across the solar disk, or "atmospheric structure types," for instance, quiet Sun, plage, sunspots, and network. This work, which can be described as solar spectrum synthesis, encompasses a series of approximations, semiempirical parameters, and detailed atmospheric models needed for computing solar spectral irradiances.

In a subsequent paper we describe in detail how these tools are combined with the analysis of solar images to obtain the spectral irradiance variations at a level of accuracy comparable with current observations. Also, we will describe how the results are used to predict values of the irradiance when only limited observations are available. Such comparisons and predictions require estimates of distributions of structure types on the solar disk at any point in time. As will be described in this subsequent paper, we compute the radiative output for each type of structure and combine this output to estimate the solar irradiance at any particular time.

The preliminary spectral samples included in the present paper do not include spectral regions that are affected by molecular species or by departures from LTE in the elemental ionization of metals. Computations of other spectral regions including these effects are in progress.

1.1. *Important Issues Related to Variability Studies*

Solar spectrum synthesis is of particular interest for wavelengths that significantly affect the chemistry and circulation in the terrestrial atmosphere. For terrestrial applications, there is need for an accurate specification of the solar radiation field as a function of wavelength and time (over timescales of days and years). The Earth's middle atmosphere (at altitude 10–100 km) is a region where the ozone chemistry is important for the atmospheric dynamics and energy balance. The solar UV radiation in the range 1800–3000 Å plays a fundamental role in the creation and destruction of ozone. Current irradiance measurements of the UV from 1170 to 4000 Å by the *Upper Atmospheric Research Satellite* (*UARS*) Solar Ultraviolet Irradiance Monitor (SUSIM) and Solar-Stellar Irradiance Comparison Experiment (SOLSTICE) spectrometers (from, respectively, Floyd et al. 1998; White et al. 1998) give necessary data for validation of results from our synthesis. The wavelength range 1000–100,000 Å contains $\sim$99.9% of the total radiative energy from the Sun and, therefore, determines the overall radiative energy input to the Earth climate system.

The properties of the upper (above 100 km) Earth's atmosphere are strongly influenced by solar EUV (at wavelengths below 1200 Å). The early irradiance measurements in the EUV by Hinteregger (1976) and Hinteregger, Fukui, & Gibson (1981) provided a rudimentary picture of solar EUV variability that will soon be improved by the *Solar and Heliospheric Observatory* (*SOHO*) observations that began in 1995. The observations in the EUV have a very substantial gap between the early and the recent observations. Even in the visible and IR regions, it is difficult to make absolute measurements with the accuracy necessary for solar variability studies. This situation drives our research into the solar spectrum calculations that can establish relationships between variations in various wavelength bands.

Table 1 shows some of the spectral features that have been already identified as important for the Earth's atmosphere.

An important question is the timescale over which changes in the solar radiation translate into relevant terrestrial timescales. The terrestrial atmosphere adjusts at different rates, depending on altitude, wavelength, latitude, etc. The continuing speculation of a link between solar and climate variability over timescales longer than decades raises the important issue of changes in the color of the solar spectrum due to variability of lines and continuum. Thus, an accurate theoretical estimate of both the solar irradiance variations and the shape of the solar radiation spectrum over many decades will help in understanding the effect of solar variability as external driver for our climate.

TABLE 1

SOLAR SPECTRAL FEATURES IMPORTANT FOR EARTH'S ATMOSPHERE

Spectral Feature	Affects
Hartley bands: 2000–3000 Å	O_3
Hertzberg continuum: ~2050 Å	O_2
Hartley bands: 2000–3000 Å	O_2
Schumann-Runge continuum: 1250–1750 Å	O_3
Schumann-Runge bands: 1750–2050 Å	O_3
H I (1216 Å, Lyα)	O_2, O_3
H I (1216 Å), He I (584 Å) and He II (304 Å)	O_2, O_3
EUV between 150 and 300 Å	NO_x
Chappuis bands: 4500–7500 Å	H_2O
Infrared: 1–2 μm	H_2O

1.2. *Theory of Stellar Atmospheres Applied to the Irradiance Problem*

In this paper we present the basic theory, approximations, and semiempirical atmospheric models that we use for computation of the line + continuum spectrum emitted by the various structures observed on the Sun. The resulting spectra are combined to obtain the Sun's irradiance spectrum. We describe the image analysis and final synthesis of the irradiance spectrum in a companion paper (Fox et al. 1999, hereafter Paper II).

A long-standing difficulty for this calculation of the solar spectral irradiance is the inclusion of the millions of lines throughout the spectrum. Extensive work was carried out by Kurucz for determining accurate data for these lines in relation with solar and stellar irradiance (see Kurucz 1992a, 1992b, 1992c, 1995; Kurucz & Bell 1995). Currently, several million lines have been accounted for, but some are still missing, particularly in the blue and near-UV spectral regions (Kurucz 1992b).

In § 2 we derive the solar irradiance from basic astrophysical theory (see, e.g., Mihalas 1978), and we discuss the various approximations we make for estimating the source functions for lines as well as continua. These approximations represent the main new features of the present computations and are critical in allowing us to obtain reasonable values of the intensity at all relevant wavelengths. We group the lines into three categories, all of them in non–local thermodynamic equilibrium (non-LTE):

1. lines in which partial redistribution (PRD) determines the wing intensities;
2. lines in which complete redistribution (CRD) is a reasonable approximation;
3. lines in which an approximate source function (as described below) is used.

TABLE 2

STRUCTURE MODELS USED FOR OUR CALCULATIONS.

Model Name	Description
A	Faint supergranule cell interior
C	Average supergranule cell interior
E	Average network
F	Bright network/faint plage
H	Average plage
P	Bright plage
S	Sunspot umbra

In this paper we do not describe in detail the cases 1 and 2, because they are described elsewhere. However, we discuss case 3 in detail because our approximation contains new elements that have not been considered previously. We introduce this approximation for estimating the source function in many lines for which it is too cumbersome to apply detailed non-LTE radiative transfer calculations with CRD or PRD. Our approximation is based on a two-level atom representation of the line source function and takes into account illumination by continuum radiation. We give a detailed derivation of this approximate method in Appendix A.

1.3. *Semiempirical Atmospheric Models for the Structures on the Solar Disk*

We construct separate atmospheric models for each of the different structures that appear on the solar disk (see Table 2). These models describe the run of various physical parameters with altitude that are needed for all relevant structures observed in the Sun. The structures associated with the solar activity cycle are sunspot and plage regions and enhanced network. However, the supergranulation cell and network lane structures in the quiet Sun also play an important role at some wavelengths. Each of these structures has been observed to have different spectral characteristics corresponding to different magnetic field configurations. These structures have different, but overlapping, brightness ranges in most wavelengths, but observationally their morphology and magnetic structure (e.g., see Harvey & White 1999) better characterize them.

The models presented here are built to represent a certain brightness level within each structure type as discussed for the *Skylab* UV data by Vernazza, Avrett, & Loeser (1981, hereafter VAL). Our models A through F are improved versions of their corresponding models for the supergranular observations. The models H and P are developed to represent two levels of brightness in plage, and model S to represent sunspot umbra.

We describe the seven model atmospheres used for our synthesis in § 3 of this paper and characterize them in Table 2. These steady state (or time-independent) models include new versions of the Fontenla et al. (1993) models. The seven models we present here include some models that were not present in FAL3, and the models in that paper have been modified to account for further observations. Our current models include hydrogen and helium diffusion in the transition region as described in FAL3. However, various improvements in the other layers (see § 3) make these transition region models somewhat different from the previous ones. Our models use some parametric approximations to determine density stratification, and we do not derive the temperature from energy-balance constraints, except in the transition region (see FAL1; FAL2; FAL3). Rather, we define the temperature in such way as to obtain agreement with the observed line and continua intensities.

In § 4 we discuss the present status of our calculations in the context of our overall goals and published work, and we show some of the results that can be directly obtained using the results from the calculations and models we describe here. We defer to Paper II the more detailed results obtained by combining the present methods and models with the analysis of solar images.

2. THEORY

The solar spectral irradiance is the radiative energy flux from the Sun through a unit surface, located at 1 AU and oriented normal to the Sun-Earth direction, and in a particular wavelength interval. An accurate computation of irradiance requires detailed accounting for all variations across the solar disk at any point in time. In the following we explain our spectral irradiance computation, its basis in radiative transfer, the scheme for including departures from LTE, and the use of the newest FAL models. We begin with a definition of basic quantities and give useful formulae relating intensities at the Sun and irradiances at the Earth. Then, we explain how we compute the solar emergent intensity and how we estimate the needed physical parameters of absorption and emissivity. Finally we give an overview of the semiempirical models we use for each structure type and describe their characteristics and heritage in solar spectral observations.

2.1. *Irradiance, Flux, and Emergent Intensity*

The specific intensity is defined as the energy crossing a unit surface, per unit time, per unit solid angle in a specified direction, per wavelength (or frequency) interval. The radiative energy flux is the vector quantity describing the energy crossing a unit receiving area oriented in a specific way (usually perpendicular to the stellar radial direction), per unit time, per wavelength (or frequency) interval. Note that while both intensity and flux are defined as energy per unit time per unit area, the two are fundamentally different. For the intensity, one identifies the direction of the radiation. For the flux, we integrate over all directions of the radiation field for a particular orientation of the surface that the radiation crosses and weight the contributions by the unit area projected on each direction of the radiation.

The emergent intensity from the solar atmosphere is defined as the energy that crosses a unit area at the solar surface (i.e., the layer of the atmosphere where optical depth is practically negligible), per unit time, per unit solid angle centered around a given observing angle, per wavelength (or frequency) unit. For the purpose of computing the emergent intensity, we assume that all the parameters of the solar atmosphere (temperature, density, atomic composition, etc.) vary only in the radial direction. Consequently, the emergent intensity at any point of the solar surface depends only on the angle between the local normal to the solar surface and the direction from which the radiation is measured. The flux or irradiance on a surface outside the Sun is computed by integrating the contributions from the entire solar disk seen from the Earth. Summation of these contributions requires the integral over the solid angle subtended by the emitting area of the Sun.

In the following, we represent the irradiance by the "average disk intensity" Ia, which is the intensity of a uniformly bright disk with the same radiative output as the Sun in the direction of the Earth. The irradiance, R, is simply related (see Appendix B) to the average disk intensity by

$$R = \Omega I_a , \tag{1}$$

where $\Omega = 6.79994 \times 10^{-5}$ sr is the solid angle subtended by the Sun at a distance of 1 AU.

Because of the gradual variation of intensity with the angle, θ, between the solar radial direction and the line of sight to the Earth (center-to-limb variation, hereafter CLV), we compute the emergent intensity, for each structure type, at 10 μ ($\mu = \cos\theta$) positions using an atmospheric model representative of each solar structure, and we interpolate the emergent intensity value for intermediate values of μ. To illustrate this approach, in Tables 3 and 4 we show the disk intensity in two wavelength regions for the seven single-component model atmospheres defined in Table 2.

The values in Tables 3 and 4 give not only the intensities as function of μ but also the average disk intensity, as defined above, for a solar disk completely covered by one of the seven surface structures and the corresponding irradiance in standard units.

The maximum Lyα irradiance is 42 mW m^{-2} for a disk filled by bright plage model (P) in Table 3. While the minimum irradiance is 2.8 mW m^{-2} for a disk filled by dark regions of the cell interior (A), for a disk filled by average brightness network cell interior (C) is 5.2 mW m^{-2}. The observed values of solar irradiance in the same spectral range at solar maximum in 1992 and minimum in 1996 are 11 mW m^{-2} and 5.8 mW m^{-2}, respectively (G. J. Rottman, G. De Toma, & T. N. Woods 1998, private communication).

The values shown in Table 4 show much smaller variations of intensity between models in the wavelength range 6070–6080 Å than the Lyα variability shown in Table 3. Here the irradiances differ between models by not more than $\sim$6%, except for sunspots, which give an irradiance -13% with respect to the quiet Sun model C. The radiation in this red band is essentially produced in the photosphere by H^- bound-free continuum.

The surface features of different brightness and the CLV of these features determine the spatial variation of the intensity at different points of the solar disk. All these variations are shown in Tables 3 and 4, but note that model E is somewhat different from the others. Also, the sunspot

TABLE 3

INTENSITIES FOR OUR STRUCTURE MODELS, INTEGRATED OVER THE BAND Lyα $\pm$4.5 Å

	μ											
MODEL	0.95	0.85	0.75	0.65	0.55	0.45	0.35	0.25	0.16	0.06	Average	TOTAL
A	4.1084	4.1064	4.1044	4.1023	4.1003	4.0955	4.0877	4.0852	4.1038	4.1249	4.1020	2.79
C	7.2829	7.3850	7.4871	7.5891	7.6911	7.9141	8.0600	8.0863	8.4955	8.6900	7.6041	5.17
E	16.439	16.681	16.924	17.167	17.410	17.670	17.949	18.207	18.315	18.293	17.134	11.65
F	23.334	23.678	24.022	24.365	24.709	25.052	25.395	25.664	25.601	25.396	24.285	16.52
H	47.562	48.111	48.660	49.209	49.757	50.236	50.641	50.851	50.341	49.709	49.001	33.32
P	62.220	62.269	62.318	62.366	62.415	62.167	61.603	60.717	59.077	57.868	62.023	42.18
S	24.713	25.276	25.840	26.403	26.966	27.846	29.064	30.778	34.169	36.874	26.740	18.18

NOTE.—Units for each value of μ and the average are 10^4 ergs s^{-1} cm^{-2} sr^{-1}. Units for the total are mW m^{-2} Å^{-1}.

TABLE 4

RED BAND INTENSITIES FOR OUR STRUCTURE MODELS, AVERAGED OVER THE BAND 6070–6080 Å

	μ											
MODEL	0.9509	0.8510	0.7511	0.6513	0.5515	0.4519	0.3524	0.2533	0.1556	0.0667	Average	TOTAL
A	3.0982	2.9451	2.7821	2.6078	2.4205	2.2181	1.9972	1.7530	1.4750	1.3018	2.5963	176.5
C	3.1034	2.9509	2.7888	2.6157	2.4299	2.2295	2.0116	1.7725	1.5053	1.3412	2.6056	177.2
E	3.0993	2.9481	2.7874	2.6159	2.4323	2.2349	2.0215	1.7892	1.5337	1.3785	2.6077	177.3
F	3.1304	2.9809	2.8223	2.6535	2.4734	2.2804	2.0729	1.8483	1.6010	1.4501	2.6472	180.0
H.....	3.1683	3.0375	2.8981	2.7488	2.5879	2.4130	2.2205	2.0045	1.7531	1.5946	2.7365	186.1
P	3.1512	3.0348	2.9092	2.7723	2.6213	2.4514	2.2550	2.0169	1.6983	1.4797	2.7448	186.6
S	0.3919	0.3651	0.3391	0.3142	0.2909	0.2693	2.2501	0.2334	0.2201	0.2135	0.3224	21.92

NOTE.—Units for each value of μ and the average are 10^6 ergs s^{-1} cm^{-2} sr^{-1}. Units for the total are mW m^{-2} $Å^{-1}$.

model shows less limb darkening than the other models because of the very steep density gradient. This model is also in development, and we discuss the sunspot model problem in § 3.2. The CLV results from the basic anisotropy of the intensity emergent from a stellar atmosphere, because of the radial variation of the temperature in the atmosphere. The temperature decrease outward in the photosphere causes the intensity formed in this region to decrease monotonically from disk center to the limb (producing limb darkening), since the intensity at the limb forms in higher layers; this is case of the red band in Table 4. However, optically thin radiation from the chromosphere-corona transition region and corona show limb brightening because of enhanced line-of-sight integration at the solar limb. Optically thick emissions lines formed in the chromosphere often do not display much variation from center to limb; this is the case for Lyα (see Table 3).

Other intensity variations across the solar disk arise from changes of the atmospheric parameters in tangential directions, but in our present work we assume that each of our component models is characterized by variations only with height.

In the following we explain our method for computing the emergent intensity at each wavelength and position on the solar disk for each of the model solar atmospheres we use for different structure types.

2.2. *Calculation of the Solar Emergent Intensity*

The formal integral solution to the radiative transfer equation is

$$I = \int_0^\infty S \exp^{-\tau} d\tau \,, \tag{2}$$

where S is the monochromatic source function and τ is the monochromatic optical depth along the line of sight. This optical depth is the integral of the total opacity, $\kappa + \sigma$,

$$\tau(x) = \int_0^x (\kappa + \sigma)\, ds \,, \tag{3}$$

where κ is the absorption coefficient (corrected for stimulated emission), σ is the monochromatic scattering coefficient, and x is the geometrical depth along the line of sight. The source function is the ratio of the total emissivity to the total opacity,

$$S = \frac{\epsilon + \sigma J}{\kappa + \sigma} \,, \tag{4}$$

where J is the local mean intensity (i.e., the intensity averaged over all directions) and ϵ is the emissivity. The atmospheric parameters ϵ, κ, and σ along the line of sight determine the variation of the coefficients in equations (3) and (4) and thereby determine the values of τ and S along the line of sight.

In the present paper, for all the structures we consider the emergent intensity is formed in a thin layer relative to the solar radius; thus, for our intensity calculations at each point of the solar surface we neglect the surface curvature and assume a tangent plane-parallel model atmosphere. In this case, the line-of-sight optical depth in equation (3) can be replaced by τ/μ, where τ is now the radial optical depth and μ is the cosine of the angle between the line of sight and the local radius. This approximation to the spherical problem breaks down very close to the limb, and for this reason we limit our calculations to $\mu = \cos\theta \leq 0.1$. At these extreme disk positions, the line of sight near the boundary of a surface structure may pass through two atmospheric models in our synthesis. However, because this effect introduces only small variations at the boundaries between surface structures, we ignore this effect and compute the emergent intensity from the source function and optical depth in the single model assigned to the feature at the solar surface. This approximation is not valid at the edges of very small solar features, but it is valid for most of the structures whose horizontal extent is much larger than the radial depth of the regions producing the observed intensity. Since we consider only medium-scale surface structures (probably composed by smaller scale features), the plane parallel approximation is adequate for our purposes.

2.3. *Calculation of Absorption Coefficient and Source Function*

Here we describe the approximations and methods we use to determine the source function and optical depth scale for each of the component models. The emphasis here is not on the synthesis of a particular set of spectral lines with high accuracy, but rather on the ability to compute broad spectral bands with sufficient accuracy to estimate the irradiance variability. Typically, these spectral bands include a few broad lines, a large number of narrow lines, and several free-bound continua. Consequently, our methods are tailored to obtaining the best estimate of the intensity in the band in a reasonable computing time, while each particular line may not be computed as exactly as might be possible by more comprehensive non-LTE calculations of all atomic and molecular constituents.

Equation (2) for the intensity is easy to integrate numerically once the source function is known as a function of the

radial optical depth. A principal problem in the synthesis of the solar spectrum for estimating the irradiance variability is an accurate accounting for the many absorption lines in the spectrum that reduce the total solar output to about 18% below the value for a line-free continuum. In synthesizing the solar spectrum, we have to consider contributions to the opacity and source function from transitions in many ions, as well as large variations with wavelength near spectral lines and free-bound absorption edges. For this reason, we must take into account all opacity and emissivity contributions at all wavelengths without resorting to wavelength averaged values. For this purpose we use the extensive lists of line opacities published by Kurucz & Bell (1995).

We compute the parameters in equation (2) at each wavelength at which an emergent intensity is needed. To increase the computational efficiency in our synthetic spectra, we compute all values on a denser wavelength grid near the lines, where the opacity and emissivity vary rapidly as functions of wavelength, to assure that the variations of opacity and source function between consecutive wavelength points are small. In particular, we compute intensities at 20 points spaced at 0.01 Å intervals around each of the identified spectral lines. Outside the lines, the point spacing opens to 0.5 Å. Because of the large number of lines in the Kurucz tabulation, there are almost no intervals free of lines. Therefore, the spacing between wavelength points rarely exceeds 0.1 Å in our calculations at UV and visible wavelengths. This dynamic spacing approach still leads to calculations at a very large number of wavelengths (about 60,000 for each 200 Å interval in the blue). An advantage of our computation is that it permits us to identify the sources of the variations easily by looking at the "zoomed in" spectra where all the line details are visible. Moreover, we can choose to include or exclude any opacity and emissivity sources in the emergent intensity calculation and, therefore, separate the effects of individual lines and continuum on the irradiance in any line blends.

Contributions to the opacity from hydrogen lines are computed in detail at any wavelength, but for the narrower lines from other elements we consider only opacity contributions from lines within 2.0 Å of the wavelength range in question. Our test runs verified that this extension around each interval is sufficient after we accounted for some broad lines, such as Ca II H and K and Mg II *h* and *k*, in a special broad-lines data file whose opacities and emissivities are always included. We take into account each of the lines contained in the most recent Kurucz & Bell (1995) CD-ROM data, but for computational efficiency we transferred these data to netCDF database files (Rew & Davis 1990; Brown et al. 1993; Rew et al. 1997). Each of our files contains spectroscopic data for all lines from one element in a spectral range 1000 Å wide. For a given spectral range, we scan our database to find all the lines contributing to the band being computed for elements up to atomic number 32 (Zn) in the periodic table. In the future we will also include molecular transitions (not included here), but molecular bands do not affect the results shown here.

We also take into account the following opacity, scattering and emissivity sources:

1. continuum sources:

a. H^-: bound-free and free-free;
b. $H2^+$: bound-free and free-free;
c. *e*: free-free;
d. H: 912 Å, 3640 Å, and higher level ionization;
e. C: edge 1100 Å;
f. Al: edge 2076 Å;
g. Si: edges 1526 Å, 1682 Å, 3880 Å;
h. Mg: edges 1620 Å, 2515 Å, 3650 Å;

2. scattering processes:

a. Thomson scattering (*e*);
b. Rayleigh scattering (H).

Our numerical models extend from the deepest observable photospheric layers that influence the visible and IR continuum to the lower coronal layers, including the transition region where the most energetic UV line and continuum emissions originate. Through this range the line and continua formation changes from practically LTE to optically thin, and several non-LTE effects may affect our calculations. Our model computations include detailed non-LTE ionization equilibrium for the most significant elements (see Vernazza et al. 1981) and effects of diffusion in the transition region. The full computations for H and He were described by Fontenla et al. (1993). Similar calculations that include diffusion in the transition region have also been applied to other elements (see, e.g., Fontenla & Avrett 1993; Fontenla 1994) and will be described in detail in a future paper.

The non-LTE effects can be separated into those that affect the elemental ionization and those that affect the level populations within each ionization stage. For simplicity, in this paper we show only sample spectra computed by assuming LTE ionization for all elements except H and H^-. We used the H ionization and level excitation from full non-LTE calculations using a 15 level H atom and diffusion as described by Fontenla et al. (1993). The atomic level excitation departures from LTE for elements other than H are discussed in § 2.3.1.

The consequences of assuming LTE elemental ionization on the particular wavelength bands we show here are not very significant, except for the emission lines in Figure 6. In most of the optical range the intensity is well described by LTE elemental ionization because it is formed in layers where the departures from LTE of the elemental ionization are small. However, some differences occur in strong absorption lines that form near the temperature minimum and whose opacities are overestimated because of the underestimation of the ionization by the LTE approach. The error of this approach becomes much larger in the upper, high-temperature, layers responsible for the UV line emissions where the ionization becomes grossly overestimated by assuming LTE. Thus, we stress that the Figure 6 is only preliminary and the intensities are not to be regarded as accurate at this point.

In future papers we will show results from including in our calculation the full non-LTE ionization including diffusion in the transition region for the most abundant elements in the solar atmosphere.

Our computational method is based on object-oriented programming (OOP) techniques. These tools permit us to easily develop, test, and use a flexible and comprehensive object library that permits to solve accurately the complicated problem of solar spectral synthesis. The C++ language was chosen because it supports OOP, is inexpensive and available on all platforms, provides high performance on all platforms, and offers very powerful low-level file access to computer resources. As an example of the applica-

tion of OOP, we mention the CAtmosphere object that encapsulates global atmospheric data, methods for input/output to text files and other global tasks, and an array of CPointHeight objects that describe all parameters at each atmospheric level. The CAtmosDB class derives from CAtmosphere and adds the capability for input/output from/to netCDF files. The code was developed, tested and debugged using Visual C++ environment on a personal computer and then ported to the Unix environment. The final programs are run in batch mode on Unix and Win32 platforms, and Windows and X-Windows based programs are used to manage the atomic data and study particular lines. A Windows program is used for carrying the complete calculation and studying the various parameters as functions of height. We use the compact netCDF archiving system for storing the Kurucz line tabulations, our current atmospheric models, and the populations computed by PANDORA (Avrett & Loesser 1992). Also, we use the netCDF format for archiving all the computed spectra.

2.3.1. *Calculation of the Line Source Function*

In deep layers where the continuum optical depth at visible wavelengths is much larger than unity, the source function is very close to the local Planck function (viz., LTE applies). Also, for the Sun (which is a relatively cool and dense star) the departure from LTE is negligible at the photospheric regions where the bulk of the emitted continuum radiation originates. Because of the radial variation of the local temperature and the wavelength variation of the opacity, the emitted spectrum departs from a blackbody spectrum at any particular temperature (see Fig. 1). Also, this temperature variation produces larger departures in spectral lines. The departures from LTE become very large in lower density and optically thin regions responsible for absorption and emission lines. Consequently, in our calculations we cannot use the Planck formula to estimate the line source function, but we require a treatment based on a more detailed analysis of the absorption and scattering coefficients. Figure 1 shows solar continuum spectra for several models compared with the Planck function (*horizontal dashed line*) at the effective temperature of the Sun, i.e., 5778 K.

We use three different approaches for obtaining realistic, non-LTE, line source functions.

1. In strong resonance lines, such as the H Lyα and Mg II *h* and *k*, we use non-LTE source functions computed with the PANDORA code with partial frequency redistribution (PRD).

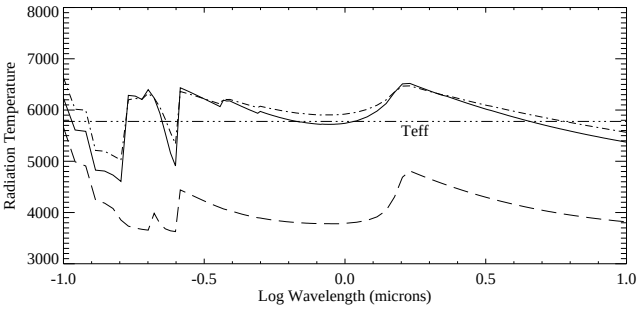

FIG. 1.—Continuum disk brightness temperature between 1000 Å and 10 μm for quiet Sun.

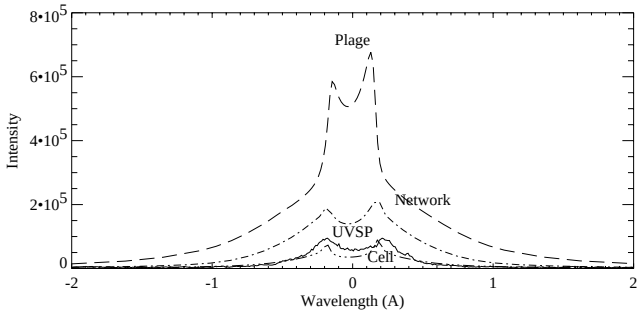

FIG. 2.—PANDORA calculations for the Lyα line profile for two quiet Sun structures, supergranulation cell center (model A) and network (model F), and for plage (model P). For reference we show a quiet-Sun observation from the UVSP instrument on board *SMM* (Fontenla et. al. 1988). All intensities are in ergs cm^{-2} s^{-1} $Å^{-1}$ sr^{-1}.

2. In other cases when the non-LTE populations from PANDORA are available but PRD is not very important, we use the computed populations and then assume complete redistribution (CRD) for our opacity and emissivity computations. This approach is used for the Balmer, Paschen, and higher Lyman lines (that use population values from a 15 level H atom PANDORA run) and for other lines where CRD is a reasonable assumption.

3. In all other cases, we compute an approximate source function based on a new formulation that uses the Planck function and a form of the "net radiative bracket" (see Appendix A) applicable to the many medium- and low-strength lines in the solar spectrum.

The three approaches we use for computing the line source function can be considered as formulations of decreasing complexity and increasing generality in specifying the source function for large numbers of spectral lines. Approach 3 is necessary because the enormous number of lines that we must consider makes it impractical to solve the non-LTE problem in full detail for all the spectral lines of all elements and ionization states found in the solar atmosphere. A simple LTE approach would give incorrect results for lines originating in the chromosphere and above. Thus, we developed our approximate non-LTE solution described in Appendix A, which we apply for most photospheric, chromospheric, and transition-region lines. This scheme for the line source function is analogous to those used by other authors (e.g., Anderson 1989, p. 575; Bohm 1960, p. 106), but our formulation contains new elements.

An example of our results using method 1 is that of the Lyα line shown in Figure 2. This figure shows computed profiles for quiet and active regions compared with the quiet Sun profile observed at high spectral resolution by the UV Spectrometer and Polarimeter (UVSP) instrument on board *SMM* (Fontenla, Reichmann, & Tandberg-Hanssen 1988).

To illustrate calculations using the method 2 we show in Figure 3 the Balmer line profiles computed in CRD using PANDORA level populations computed for model C at disk center. For reference we also show the observed profiles from Debouille et al. (1981).

Figure 4 illustrates our approach 3 in an extreme case of a low chromospheric line, we compute the source function for the Ca II K line using this approximation and various ways of estimating the net-radiative bracket. In this figure

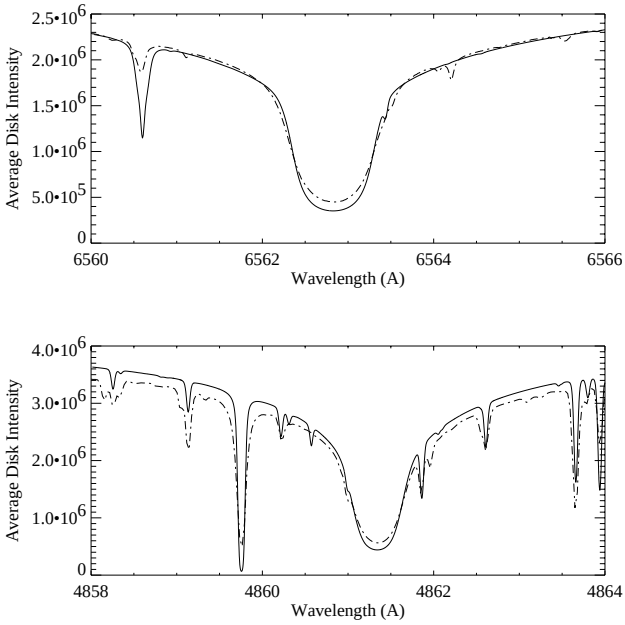

FIG. 3.—Average disk intensity spectra of the first two Balmer lines: calculated (*solid line*) and observed (*dashed line*). Intensity is in ergs cm^{-2} s^{-1} $Å^{-1}$ sr^{-1} and the observed spectrum was normalized to match the theoretical continuum far away from the lines.

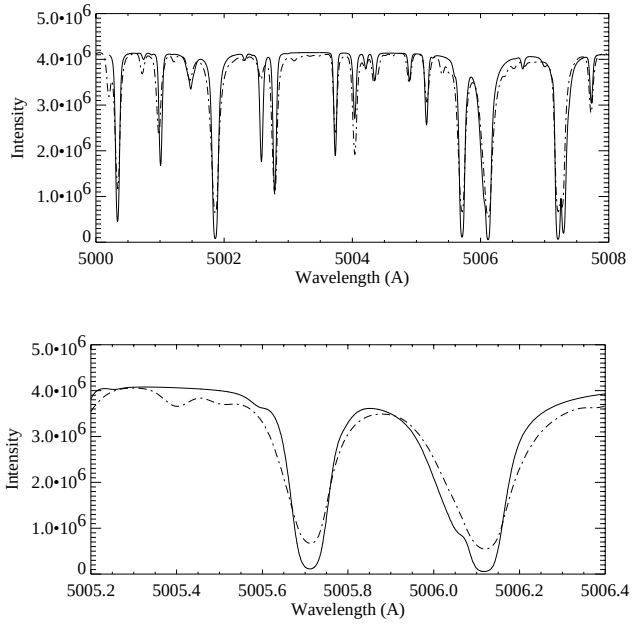

FIG. 5.—Computed spectrum (*solid line*) for the quiet Sun (model C) (*upper panel*) at disk center between 5000 and 5008 Å and (*lower panel*) the detailed profiles between 5005.2 and 5006.4 Å. The dashed line shows the observed spectrum (Debouille et al. 1981) normalized to match the computed continuum intensity. Intensity is in ergs cm^{-2} s^{-1} $Å^{-1}$ sr^{-1}.

we also show the LTE (i.e., with the Planck function of the local temperature), optically thin approach, and full non-LTE and PRD calculations using PANDORA in Figure 4.

The cases shown in this figure by the dash–triple-dotted, dashed, and dot-dashed lines use the expression

$$S_{\rm lin} = \frac{\zeta B + C}{\rho + \zeta + \chi}, \tag{5}$$

where ζ is the ratio of the collisional to spontaneous deexcitation, B is the Planck function, ρ is an estimate of the net radiative bracket (see Appendix A), and χ and C are coefficients that represent the continuum contributions (see Appendix A). The simplest approximation for ρ is to assume that this coefficient is given by the second exponential integral function of the line center optical depth. This expression results from the theory for a homogeneous source function atmosphere. Clearly, this expression of ρ underestimates the net radiative bracket at large optical depths because it does not account for the photon escape through the line wings. A more correct expression is to integrate the previous value over the line profile; however, this integral involves too much computation when carried for all the hundreds of thousands of lines in many spectral ranges. Thus, we adopt for our approach 3 the approximation discussed in Appendix A, which gives the result shown by the dot-dashed line in Figure 4. This approximates the integral mentioned above and provides a reasonably good approximation to most of the solar lines in all atmospheric layers. The result shown by the long-dashed line obtained using an optically thin approximation assumes $\rho = 1$ and clearly underestimates the source function. In the cases shown by the dashed, dot-dashed, and long-dashed lines here, we included the same continuum terms described in detail in Appendix A.

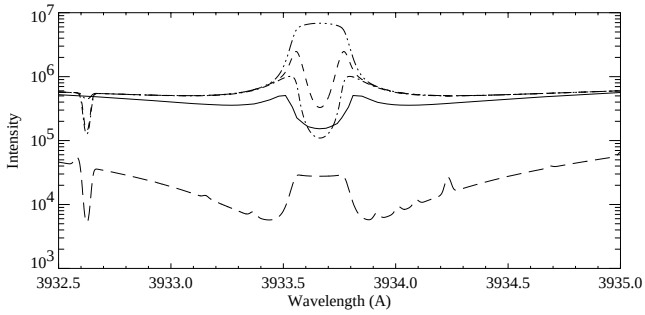

FIG. 4.—Comparison of five methods for computing the Ca II K line profile for the quiet Sun model (C). The profiles are, from top to bottom: assuming LTE (*dash–triple-dotted line*); assuming the net radiative bracket given by the second exponential integral function of the line center optical depth (*dashed line*); our approximation for the net radiative bracket (*dot-dashed line*; see Appendix A); the full calculation carried with PANDORA using PRD (*solid line*); and the optically thin, approximation for the line source function (*long-dashed line*).

The Ca II resonance lines are included in our broad-lines category and computed as in procedure 1 described above. We show the comparison in Figure 4 to indicate that the approximation we used for the thousands of narrow lines in the spectra is not far from a full non-LTE result in most cases, and it is not far off even in the extreme case of the Ca II K line.

Finally, in Figures 5 and 6 we show samples of our computed spectra. The magnified panels show the level of detail present in our synthetic spectra.

Using these results we construct spectra databases (again in the netCDF format) containing data such as that shown in Figures 5 and 6, computed at 10 values of μ to account for limb darkening and for up to 10 types solar surface features (we are currently using only 7 types). These files contain all data needed for the irradiance calculations we describe in subsequent papers.

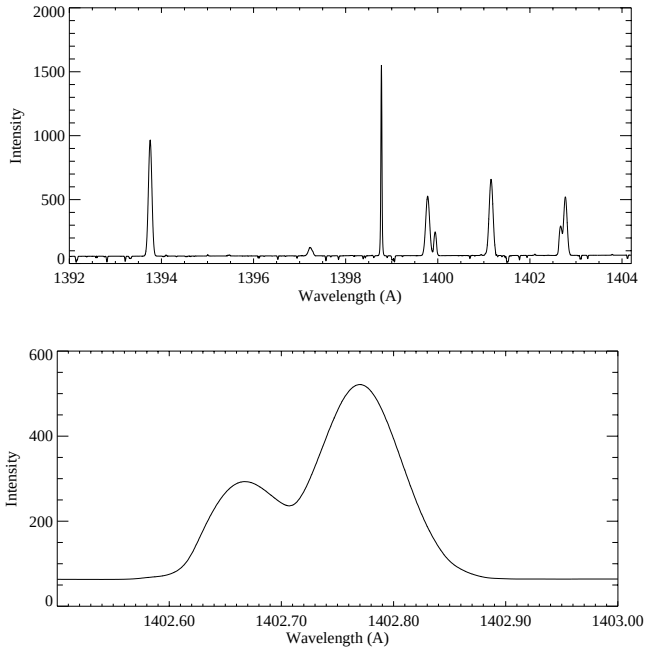

FIG. 6.—*Upper panel*: Computed spectrum for the quiet Sun (model C) at disk center between 1392 and 1406 Å. This spectral region is a mixture of strong emissions lines and weak absorption lines. *Lower panel*: Detailed profile of the Si I-Si IV blend. Intensity is in ergs cm^{-2} s^{-1} $Å^{-1}$ sr^{-1}.

3. ATMOSPHERIC MODELS

In order to compute the emergent intensity for the most common solar surface structures, we use seven semiempirical atmospheric models. These models describe the depth-dependent physical conditions in the set of steady state (or time-invariant), one-dimensional numerical models. The use of one-dimensional models for the coarse structure of the Sun is justified because the relevant surface features are substantially more extended across the disk than in depth. For example, compare the density scale height of a few hundred kilometers to the extent of, say, network lanes of several thousand kilometers. Our use of a set of predefined steady state models implies that the irradiance variability estimated from our synthesis arises from the variation in distributions of the various structures covering the visible disk at any one time.

The radial variation of the physical parameters (temperature, density, etc.) characteristic of these solar features can be inferred only from an analysis of the observed emergent intensity on a feature by feature basis. Such an analysis is carried out in a different way depending on the spectral signatures of each structure and leads to specific models of the radial variations of temperature, density, and other parameters for the different solar surface structures. These models provide the physical quantities needed to compute the emitted spectrum. As usual, the calculation utilizes an intermediate set of physical parameters, namely, the radiative emissivity ϵ, the absorption coefficient κ, and scattering coefficient σ.

These models are then the basis for our synthesis of the solar spectrum at any disk position out to $\mu = 0.1$ and from millimetric to near UV wavelengths without any large gaps.

The use of steady state models does not imply that all dynamic phenomena are neglected, but only that the temporal variability is not considered in detail. Our calculations include several types of velocities.

1. Microturbulent velocities that are customarily used in astrophysics for reconciling observed line widths with those computed, describing averaged values of random velocities.
2. Turbulent pressure velocities that are ad hoc quantities describing a temporal average density stratification smoother than that expected in strict hydrostatic equilibrium. See Vernazza et al. (1981) and FAL1. Currently these values are set equal to the microturbulent velocity values.
3. Diffusion velocities that affect the H and He ionization (see FAL1; FAL2; FAL3).
4. Steady flow velocities that also affect the density stratification and the ionization balance and produce line shifts.

Thus, the models we consider cannot be properly called hydrostatic, because they include dynamic processes through terms that represent these phenomena. However, our models do not include any terms containing temporal derivatives. Our current models are not fully self-consistent theoretical physical models but rather are semiempirical models derived to reproduce particular sets of observations. These models have terms with a qualitative physical basis for representing physical dynamic phenomena that are not yet completely understood. The reason for this choice is that, for the present synthesis, our primary concern is a snapshot of the solar irradiance. Here, we focus on accurately reproducing the daily-averaged spectra in our set of surface structures, and we rely on future advances to produce a theoretically consistent picture of all the phenomena in the solar atmosphere. Furthermore, no physically consistent models that reproduce all the observed spectral features from the photosphere to the base of the corona are currently available. The available dynamic models are still sketchy and lack the opacity data and non-LTE effects that are included here. Also, the dynamic models proposed so far do not consider the three-dimensional magnetic field that determines the chromospheric and coronal heating and the complicated structure and phenomena as observed in Hα and in coronal and transition region lines. Our methods are developed in such way as to include, as they become available, improved theoretical models able to explain the spectra of the observed structures.

We ignore the presence of dynamic elongated features, such as spicules, macrospicules, and prominences, that create a "jungle" of structures observed at the limb (Kiepenheuer 1953; Athay 1976, p. 52). Although very prominent at the limb, their effects on the spectral irradiance are minor. Besides, most of these features are highly dynamic, time dependent, and affected by the magnetic field. Consequently, taking them in consideration would require statistical MHD models in which the temporal average for the ensemble of features adequately accounts for the effects of the dynamics on the lines and continua. Such comprehensive models are not yet available.

The atmospheric models used here originate from the first given by Vernazza et al. (1981), subsequently modified as discussed by Avrett (1985, 1990), and further improved by Fontenla et al. (1989, 1992, 1993). See Avrett (1998) for a recent review.

Our semiempirical models, constructed in the course of this irradiance study, contain significant improvements over the previous ones by FAL3, FAL2, and FAL1, and even

more substantial changes over the preceding VAL model series. Thus, the current models should not be confused with the VAL models that, although the best at their time, did not fit several observations well, in particular the H, He I and II resonance line profiles. In FAL models we retained, for simplicity, the chromospheric temperature distribution determined earlier from EUV observations by Vernazza & Reeves (1981) even though the new FAL3 transition-region structure requires modifications of the chromospheric temperatures in order to retain agreement with the EUV observations. The models given here include these adjustments of the chromospheric temperature distribution as well as other adjustments to improve agreement with observations.

Our semiempirical models are constructed to reproduce observed emergent intensities and profiles at wavelengths from the UV to radio wavelengths. Thus, we expect intensities computed from these models to give reasonable absolute intensities and, hence, good irradiance estimates. The current set of models is shown in Figure 7 and is available on request.

The transition-region portions of these models are very sharp and are determined theoretically in that the temperature variation with height, $T(z)$, is calculated from the hypothesis that the radiative losses are compensated by the downward energy flux from the corona (see FAL1; FAL2; FAL3). These transition-region models have only two physical constraints [the pressure and slope of $T(z)$ at the base of the computed region] and are in good agreement with the UV Lyα and He line profiles. We believe that the reason for their success compared to the previous models is that the FAL models of the lower transition-region consider H and He particle diffusion for the first time and compute this process consistently with particle transport theory. Consequently, we warn the reader against mistakenly using emission-measure methods that do not include particle diffusion and are inconsistent with the models we use. In subsequent papers we will show the computation of the ionization of various elements considering particle diffusion. Here we just mention that calculations using model C and these methods give good agreement between computed C IV resonance lines and the observed ones.

In the following we briefly describe the background of the models to emphasize which features of the solar spectrum lead to estimates of physical conditions at different layers.

3.1. *Photospheric Layers*

The photospheric parts of the models are derived from the observed continua in the visible and IR spectrum between 3100 Å and 10 μm. The early models (see, e.g., Gingerich et al. 1971; Holweger 1967; Holweger & Muller 1974) were based on LTE line and continuum intensities at optical wavelengths for the average quiet Sun observed at low spatial resolution and on center-to-limb data. These models showed H^- to be the most important opacity source in the visible and near IR spectrum. Also, they showed that the solar photosphere, on average, is very close to radiative equilibrium but has a small departure from this condition caused by dynamic energy transport in the convection overshoot layers.

More recent models account for variations due to sunspots and plage. Maltby et al. (1986), Lites & Skumanich (1992), and others proposed sunspot models. Collados et al. (1994) present further work on sunspot models, and we stress that the current models are far from definitive. Our sunspot umbra model is similar to these models in the photosphere and is extended into the upper layers as discussed in the next section. Our plage model is based in part on the results from Shine & Linksy (1974) and Lemaire et al. (1981). We modified the temperature distributions in the

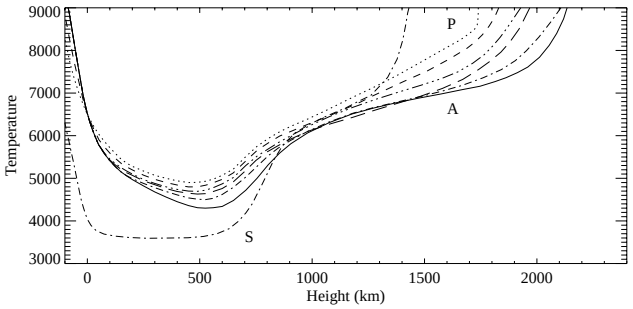

FIG. 7*a*

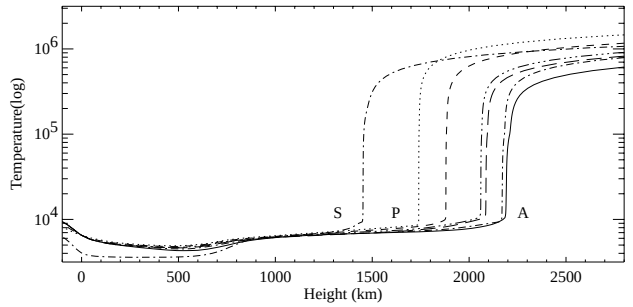

FIG. 7*b*

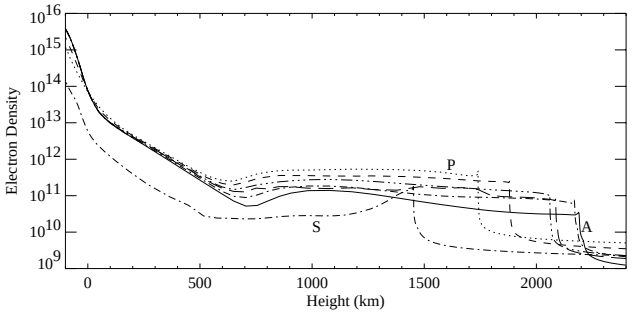

FIG. 7*c*

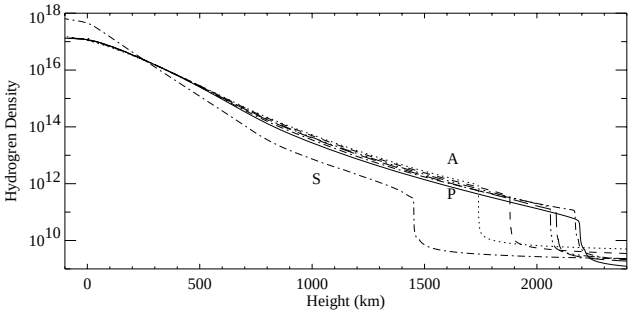

FIG. 7*d*

FIG. 7.—(*a*) Temperature as function of height for our models. (*b*) Logarithm of the temperature as function of height for our models. (*c*) Electron density as function of height for our models. (*d*) Hydrogen density as function of height for our models.

deep photospheric layers of our plage models, P and H, relative to the quiet Sun models. These modifications were determined in order to reproduce the center-to-limb variation and facular contrast observed at 1.6 μm by Foukal et al. (1990) and the measurements by Topka, Tarbell, & Title (1992, 1997) and Wang et al. (1998). At all heights, these temperature differences are small; however, they have significant effect on the total solar irradiance. Since photospheric radiation dominates the total radiative output of the Sun, continued improvement in photospheric models will improve the synthesis of the solar output.

The photospheric layers are defined here as those where the visible continuum is formed. The analysis of the spectra of individual surface structure types cannot provide an absolute height scale. Consequently, it is customary to define the arbitrary zero height of the stellar atmosphere as the radius at which $\tau_{5000} = 1$, where τ_{5000} is the continuum optical depth at 5000 Å for a radial line of sight. Thus, the photospheric layers of each of the models extend from about 80 km below to about 300 km above this zero level.

We stress that our models do not have an absolute height reference, and heights are measured for each model independently of the others. This is a direct consequence of the inability of the spectroscopic methods to establish an absolute height scale and the fact that it is unknown what the offset may be between the layers where $\tau_{5000} = 1$ occurs in the various models. However, because of lateral force balance, we do not expect the arbitrary zero levels of all seven models to be more than a few hundred kilometers apart. This uncertainty has no effect on our calculation of the intensities.

The photospheric models assume a density stratification that departs somewhat from hydrostatic equilibrium because of the Bernoulli term, with velocity ~ 2 km s^{-1}, that represents the dynamical contribution to the momentum balance equation.

The main opacity source for the IR and visible continuum is H^- with its free-bound and free-free contributions. These combine in such way as to have a minimum at 1.6 μm wavelength. Thus, observations around this wavelength determine the deepest layers of our models. The H^- free-free opacity increases toward larger wavelengths and provides ways for estimating the photospheric temperature decrease with height. Near 8000 Å [log (wavelength) $= -0.1$ in Fig. 1] the H^- opacity (bound-free) has a maximum (see Aller 1963)) that results in a local minimum of the observed irradiance brightness temperature (see Fig. 1). At shorter wavelengths, in the blue, the H^- opacity decreases, but free-bound absorption in hydrogen and neutral metals becomes important below 4000 Å [log (wavelength) $= -0.4$ in Fig. 1]. In this spectral region, the bound-bound absorption of the millions of metallic lines becomes a dominant opacity source.

3.2. *Low Chromospheric Layers*

The low chromosphere layers are defined here as extending from the top of the photosphere (at about 200 km height) up to the temperature minimum at about 500 km height. For all models, except the sunspot model, the temperature minimum occurs near 500 km above the $\tau_{5000} = 1$ layer. In the sunspot model the low-temperature region is much colder and extends from 100 to 500 km. The plage models have substantially higher temperatures than the quiet Sun models. This temperature increase is necessary to obtain agreement between the computed intensities and observed enhancements in the Ca II and Mg II line wings and the UV continuum. We note that the Balmer absorption lines are observed to be broader in plage and network than in the quiet Sun, and this produces a negative contrast in off-band images for network and plage, a feature that is also reproduced by our present calculations.

These low-chromospheric layers are mostly transparent in the IR and visible continuum spectra, but they have very significant continuum opacity in the near UV. The low chromosphere significantly decreases the radiative output in the visible because of the numerous absorption lines first identified by Wollaston (1802) and Fraunhofer (1817). These layers have been extensively studied by measuring and modeling the absorption lines under the assumption of LTE (see Holweger 1967; Holweger & Muller 1974).

In the UV from 1100 to 4000 A, several bound-free absorption edges and particularly those of Mg and Al (see § 2.3 above) raise the height at which this continuum radiation forms to near the temperature minimum. Recent observations of the UV continuum give improved estimates of the temperature in these layers and basically agree with the current models.

Single-component models for each structure type account reasonably well for the narrow lines in the visible and IR spectra. An exception is in the CO lines. Two-component models have been proposed to interpret these observations (Ayres & Weidemann 1989; Ayres 1995; Avrett 1995); but recent observations by Uitenbroeck, Noyes, & Rabin (1994) show that the strong CO lines are highly time dependent on small spatial scales, suggesting that the CO absorption is strongest at times when the plasma is coolest because of the passage of wave disturbances through the atmosphere. Consequently, the explanation of the CO line strengths may need to consider multidimensional and time-dependent effects that are beyond the scope of the present paper.

Our sunspot umbra model departs dramatically from the other models in the low chromosphere and has a more extended and deeper temperature minimum. This model is derived from IR continuum data and lines in the visible but is also compatible with the available UV continuum data (e.g., Gurman 1984). However, sunspots are not all alike, and substantial variations appear from one to another and even within the umbra of a given sunspot. We base our model on the umbral core model M from Maltby et al. (1986), which applies to sunspots with large umbrae and well-developed penumbrae. A drawback of our sunspot models is that they do not consider flows or a divergence of the magnetic field. Both effects substantially affect the variation of density with height, but they have not yet been consistently modeled. Thus, the height scale of our sunspot model is not well established, and the temperature as a function of optical depth or column mass is more reliable. Also, our models do not yet include a penumbra as a separate surface structure.

3.3. *Upper Chromospheric Layers*

We consider this region as that where the temperature rises from the minimum and reaches an extended plateau at values between 6000 and 8000 K. The upper chromosphere extends up to a height of 1500–2200 km above the zero level (depending on the structure considered). The upper chromosphere is far more variable than the low chromosphere, and this variability appears to be closely related to

magnetic fields. In Hα narrowband data, the upper chromosphere appears as a "jungle" of more or less elongated structures resembling short loops and a pattern of dark "rosette" and "spicule" structures in the magnetic network. This is more evident in plage, where the data shows long "fibrils" connecting opposite magnetic polarity regions. Our models cannot account for this fine structure but describe only average characteristics of the upper chromosphere, weighted by their effects on the most important lines and continua formed there.

Our models of the upper chromosphere are less certain than those of the lower chromosphere. While the upper-chromosphere contribution to the total solar irradiance is less than 5%, this region is important in the near UV. The upper chromosphere was first seen in the emission lines visible in the eclipse flash spectrum. The He I 5876 Å line is one of the lines that are rarely visible as weak absorption on the disk but is a strong emission line in the flash spectrum. In the near UV, the upper-chromosphere layers produce a complicated mix of absorption and emission lines that are hard to discern in the region from 1700 to 2000 Å. Space observations show the upper-chromospheric structure in Lyα (this line has also a transition-region component; see FAL 2; FAL3), the Mg II *h* and *k* emission cores, and the free-bound Lyman, C I and He I continua (see VAL 3). The temperature structure of these layers is derived mainly from lines and continua mentioned above. Since these emissions form in low-density layers and, consequently, have large departures from LTE, the models are more difficult to construct and require non-LTE calculations.

Coronal UV and X-rays illuminate the upper chromosphere, particularly near active regions with dense coronal loop structures. This external radiation increases the ionization of some elements above that, which would result in its absence. This is particularly true for helium, in which the increased ionization leads to an overpopulation of the triplet levels that enhances the 10,830 Å line absorption. This line forms throughout the upper chromosphere as the radiatively ionized He recombines into the triplet levels and greatly increases this line absorption in plage regions, as shown by Avrett, Fontenla, & Loeser (1994).

The cores of the Ca II H and K resonance lines form at the bottom of the upper chromosphere and the double-peaked emission is very faint in quiet regions of the Sun. While these line cores are insignificant contributors to the irradiance, indices computed from the line core intensities are used for algorithms that estimate the UV irradiance and the effects of solar activity on the radiative output of the Sun. These line core emissions have very strong increases in network lanes and, especially, in plage where the emission is more than twice that in quiet regions. The emissions are well correlated spatially with the magnetic fields measured in the underlying photospheric layers. The Hα line core forms essentially through the entire chromospheric temperature plateau and shows only a few percent increase in plage. In contrast, the UV lines formed in the upper chromosphere have large differences between the various structures, and their brightness correlates with the magnetic field. The velocities (at least at the available resolution) are less important in the bright magnetic regions, as shown by the smaller asymmetries and broadening observed in the UV lines at the brightest locations (Fontenla et al. 1989).

Also, most upper-chromospheric UV lines display narrower profiles and smaller central reversal in the network and plage. These features are accounted for in our plage models P and H, and our network model F, and determine the extent of the chromospheric plateau, which is smaller for plage and network than for quiet Sun. In the sunspot models the upper chromosphere must have a very small extent to account for the lack of central reversal and narrow (but bright) cores of the observed Ca II H and K, Mg II *h* and *k* (Gurman 1984), and Lyα (Fontenla et al. 1988) lines. Our upper-chromospheric sunspot model profiles approximate these observed profiles, but the upper-chromospheric sunspot model still needs improvement.

Our models explain most of the main features of the emergent intensities for the plage, network, sunspot, and quiet Sun structures, but they do not explain transient rapid variability and associated velocities. Thus, our models give only time-averaged intensities, which are suitable for solar irradiance estimates. We also note that the parameters in our models, especially the temperature, are not obtained as any temporal averaged quantity but rather as "effective" values chosen to reproduce the observed spectra. It is not obvious that this approach should yield agreement at all wavelengths, but from the comparisons with available observations we conclude that our semiempirical modeling is able to reproduce most observed spectral features.

Magnetic fields must not be neglected in theoretical modeling of the upper chromosphere and above because they are closely related to the bright network and plage and are important in chromospheric heating. Moreover, magnetic fields are closely related to the upper-chromospheric dynamics and heating, e.g., spicules and microflares (Porter, Fontenla, & Simnett 1995). Consequently, we believe that theoretical modeling of the upper chromosphere must be based on magnetohydrodynamic computations to explain all the observations and chromospheric heating relevant to the solar irradiance. Until such theoretical models are achieved, it is premature to attempt using any dynamic models (other than semiempirical ones) to compute UV irradiances.

3.4. *Lower Transition Region*

The lower transition region is defined as the region of a steep rise of temperature with height. In this region the temperature rises from the chromospheric plateau at 6,000–7,000 K up to about 100,000 K. The geometrical thickness of this region is typically a few kilometers up to tens of kilometers. Again we caution against using inconsistent emission measure techniques for determining emissions from our models.

Our models of the lower transition region are based on a more complete physical picture than the models for lower layers. As the FAL papers explain, the energetics of this narrow region is likely dominated by the balance between the energy downflow from the corona and the relatively large (per unit volume or mass) radiative losses mainly from H and He. In these layers, steady state modeling is a good approximation because the very small acoustic transit time quickly builds an almost constant pressure (modified by the Bernoulli term; see FAL 1). Also, the very rapid cooling/heating time due to the efficient radiative losses and ionization energy transport quickly leads to an equilibrium, steady state temperature distribution. The steep ionization gradient makes it very important to include particle diffusion in determining the H and He ionization and the ioniza-

tion energy flow (see FAL 1; FAL2; FAL3). The small geometrical thickness of this layer makes the effects of a passive magnetic field divergence negligible and makes particle diffusion important in ionization balance and ionization-energy transport. All the transport effects make this layer much less sensitive to the details of the local heating and much more sensitive to the boundary conditions than the chromospheric layers of the atmosphere.

Thus, our lower transition-region models are computed from the assumed lower boundary conditions (base pressure, temperature and temperature gradient) and basic physical constraints such as pressure and energy equilibrium. These models have few arbitrary constraints, and their success in explaining the observations supports the validity of our basic physical assumptions. We have slightly modified the FAL 3 models in order to fit the observed H and He lines profiles better. These improvements are coupled with variations in the upper chromosphere and consist of slight changes to the height of the start of energy-balance calculations used to determine the temperature variation with height. Such changes translate into changes of the pressure of the transition region and changes to the temperature and its gradient at the lower boundary of the calculation.

Several UV emission lines form in this region, and the most important are the Lyα, Lyβ, and He I and II lines (the Lyα and He I lines have also upper chromospheric contributions). The UVSP instrument on board *SMM* had reasonable absolute calibration and observed the Lyα line extensively (Fontenla et al. 1988). This line is one of the major constraints of our models that reproduce well the total intensity, high-resolution profiles, and variability. The variability of the total Lyα emission is shown in Table 2 and agrees with the irradiance measurements carried out by the SOLSTICE instrument given by Rottman, Woods, & Sparn (1993) and G. J. Rottman, G. De Toma, & T. N. Woods (1998, private communication).

As reported by Fontenla et al. (1988, 1989) and observed in *SOHO* images, most of these lines show dynamic elongated structures and prominences above the limb. These features are somewhat similar to those mentioned above in Hα. Also, diffuse, very faint emission is observed in Lyα from the corona. However, the structures above the bright rim observed at the limb (see below) are faint and do not contribute significantly to the solar irradiance. In the present paper we do not consider these structures above the limb.

3.5. *Upper Transition Region*

This region of the atmosphere extends from temperature $\sim$100,000 K up to coronal values of about 1.5 MK, and for all models used here the temperature logarithmic gradient decreases monotonically from the steep gradient to the nearly uniform coronal temperature. This region produces a number of emission lines in the UV spectra, such as the Si IV $\lambda\lambda$1393, 1402 and C IV $\lambda\lambda$1548, 1551 resonance line pairs. Also, many EUV lines of high-ionization elements are formed in this region, and this radiation has significant effects on the H and He ionization in the upper chromosphere. The contribution of the upper transition region lines to the irradiance is small, but their large variability may affect the Earth's upper atmosphere. The total radiative output by the lines formed in the upper transition region is at most an order of magnitude smaller than the radiative losses from the lower transition region. These lines show extremely large (several orders of magnitude) increases of the intensity in magnetic active regions on the Sun. Thus, although the radiative output of this region is very small, the variability of this output is very large.

A simple model for this region is that of the footpoints of overarching coronal loops. This model is strongly suggested by the bright narrow rim at the limb of the Sun that was shown by *Skylab* images. The intensity in this rim is several times higher than that on the disk, and indicates a small range in height of formation and important projection effects at the limb. The projection effects are so important in these lines because their formation regions are optically and geometrically thin on the disk, and at the limb the photons generated throughout the very long tangent line of sight accumulate and produce much higher intensities than on the disk.

Our current models of this region are extrapolations from the lower transition-region models, again using the constraint of energy balance between the energy downflow and the radiative losses. However, in contrast to the lower transition region, the energy downflow is given only by the Spitzer (1962) electron conductive flux because H and He are fully ionized. The radiative losses were taken from Cox & Tucker (1969). This is a preliminary approach because, owing to the steep temperature gradient and the low density, it is necessary to consider the particle diffusion and abundance variations in all relevant elements and to use many UV line observations to improve this model. The diffusion and abundance effects, in turn, affect the radiative losses and make these losses much more complicated to evaluate. Completely consistent models have not yet been carried out, and they are important for computing emissions from the upper transition region.

4. SUMMARY

In this paper we have introduced the theory, methods, and models that we use to compute the solar spectrum and the irradiance affecting the Earth's atmosphere. These calculations are used in combination with solar image analysis for computing the spectral irradiances and its variations in future papers. The code used here is written in C++ and takes advantage of the object-oriented technique for designing a module library. These modules are combined in different in the programs that we use in our calculations.

In this paper we reviewed the basic definitions of intensities and fluxes and the relevant stellar spectra theory that we will use in Paper II for studying the variations of irradiance at the Earth that result from changes in the distributions of typical structures on the solar disk. We also described our treatment of the opacity and source function that is critical for our results. In order to consider non-LTE effects in many lines, for which it is impractical to solve in full detail the non-LTE statistical equilibrium, we introduce a new formulation of the source function that is described in full detail in Appendix A.

Combining this new approximation with full multilevel calculations with PRD for strong resonance lines and CRD for weaker lines, we obtain a description of the different excitation regimes that approximately reproduces the solar spectrum. Thus, we are now able to study the combined

variability of the continuum and the millions of lines in the spectrum, especially in the range below 5000 Å. For ranges above this wavelength, our methods also apply but the effects of the lines become less pronounced.

These methods utilize the extensive Kurucz tables of atomic lines for computing spectral bands from the EUV to the IR. One important feature of our approach is the detailed treatment of the opacity and emissivity variation with wavelength. As was described above, at any wavelength, we sum opacities and emissivities from the appropriate transitions in all ions listed in the Kurucz tables. Our calculations use seven new semiempirical models for the characteristic solar structures observed on the disk. These new models have variations in the gradient of the temperature distributions in the deep photosphere to account for the variation in plage contrast with wavelength and disk position. Also, we have introduced a number of improvements over our previous models.

To illustrate the results from these calculations, we weight the "pseudo"-Sun irradiances in Tables 2 and 3, and others not shown, by typical values for the fractional areas of each structure type at solar maximum and minimum, and we compute several bands from 1216 Å to 2.2 μm. The values in Table 5 for typical fractional areas for the various structures result from our experience with *SMM*/UVSP spectra (Fontenla et al. 1988) and analysis of Ca II K images (Fox et al. 1999). Table 6 shows the result of this simple computation. We also show in Table 6 the corresponding Lyα irradiances from the *UARS*/SOLSTICE experiment and the Neckel & Labs (1984) observations. Finally, in Table 6 we list the percentage variations about the quiet Sun values that result from the distributions of the seven structures as shown in Table 5 for two levels of solar activity.

Columns 2 and 3 in Table 6 show the agreement between the quiet-Sun computed and observed irradiance is within 3% for Lyα, a chromospheric/lower transition region line. The departure of our calculations from the Neckel & Labs (1984) data for the photospheric bands is 3% or better in the near IR wavelengths at 8650 Å and less than 1% in the red

TABLE 5

PROPOSED RELATIVE AREAS FOR THE MODELS

Model	Solar Structure Type	Quiet Sun	Active Sun, Small Plage Area	Active Sun, Large Plage Area
A	Faint supergranule cell interior	0.10	0.09	0.08
C	Average supergranule cell interior	0.77	0.70	0.67
E	Average network	0.10	0.09	0.10
F	Bright network/ faint plage	0.03	0.06	0.07
H.....	Average plage	0	0.05	0.05
P	Bright plage	0	0.007	0.026
S	Sunspot umbra	0	0.003	0.004

TABLE 6

OBSERVED AND COMPUTED SOLAR IRRADIANCES, AND IRRADIANCE CHANGES FOR SOLAR CYCLE

Spectral Band	Quiet Sun Computed (mW m^{-2} $Å^{-1}$)	Quiet Sun Observed (mW m^{-2} $Å^{-1}$)	Active Sun Small Plage Area (% increase)	Active Sun Large Plage Area (% increase)
Lyα $\pm$ 4.5 Å	5.92	6.0	34.0	49.0
4095 $\pm$ 5 Å	203.2	170.8	0.002	0.006
4105 $\pm$ 5 Å	164.2	150.4	0.06	0.10
4115 $\pm$ 5 Å	208.4	182.2	−0.04	−0.06
4925 $\pm$ 5 Å	198.1	190.1	0.09	0.14
4935 $\pm$ 5 Å	197.9	189.3	0.10	0.15
4945 $\pm$ 5 Å	205.5	206.3	0.06	0.09
4955 $\pm$ 5 Å	200.3	193.1	0.08	0.12
4965 $\pm$ 5 Å	202.0	202.2	0.08	0.12
4975 $\pm$ 5 Å	203.8	202.3	0.08	0.12
4985 $\pm$ 5 Å	188.0	187.1	0.11	0.18
4995 $\pm$ 5 Å	201.9	197.5	0.07	0.10
5005 $\pm$ 5 Å	197.4	186.2	0.06	0.09
6065 $\pm$ 5 Å	177.1	176.4	0.08	0.11
6075 $\pm$ 5 Å	177.2	176.2	0.08	0.11
6085 $\pm$ 5 Å	173.4	174.7	0.10	0.15
8530 $\pm$ 10 Å.....	94.10	97.4	0.18	0.26
8550 $\pm$ 10 Å.....	85.48	87.8	0.32	0.46
8570 $\pm$ 10 Å.....	99.69	101.2	0.11	0.14
1.3–2.2 μm	...[a]	Uncertain	−0.13	−0.17

NOTES.—Observed values are from Neckel & Labs 1984, except for Lyα, which is from Rottman et al. 1993 and G. J. Rottman, G. De Toma, & T. N. Woods 1998, private communication.

[a] The ratio of the irradiance in the band to the total irradiance is 0.14132.

at 6080 Å. However, it is between 9% and 19% for some wavelengths of the blue 4100 Å band, in which our calculations yield values substantially larger than the observed. When the detailed spectra is studied, it becomes clear that these discrepancies are due to missing absorption lines in our synthetic spectra.

Note that our scheme yields intensities and irradiances in absolute units. We stress that the agreement between observed and computed quiet Sun irradiances is not forced by arbitrary parameters. Rather, this agreement results from the observational basis of the semiempirical models; i.e., they are constructed to reproduce observations of absolute intensities in lines and continua made in many past observations.

We obtain initial estimates of the solar cycle variability for the bands in Table 6 by using the fractional area contributions by each structure corresponding to the quiet Sun reference and two levels of activity given in Table 5. The fourth and fifth columns of Table 6 give our estimates of the percentage changes in spectral irradiances for Lyα and in five bands from 4100 Å to 2 μm for two levels of solar activity defined by Table 5. The Lyα irradiance increases by 34% and 49% from solar minimum to maximum. Our quiet Sun value is within 3% of the observed value and our high activity value is below the observed by 20%. The difference with the observations at maximum solar activity may be due to underestimating the plage area, which is often larger in Lyα than in Ca II lines. The sample wavelengths between 4100 Å and 8600 Å show irradiance changes ranging from -0.04% to 0.46%. The solar cycle variation in the photospheric bands is very sensitive to the presence of strong lines, as is observed, away from them the variation is close to the published estimates of $\sim 0.1\%$. The difference may be explained by an overestimate of the plage area in the photospheric layers. The irradiance in the band from 1.3 to 2.2 μm decreases by 0.13% to 0.17% with increasing activity. This change in the sense of variability between visible and infrared wavelengths is due to the lower temperature and opacity in the deep photosphere for plages.

These comparisons are consistent with the observations indicating that brighter areas that our plage models describe are more extended, or have a higher filling factor, at the upper-chromospheric layers and their extension reduces monotonically as one approaches the photospheric layers. Basically this is equivalent to a "canopy" effect that has been suggested from other observations. Quantitative studies of the variation of the plage filling factor could produce scaling factors that improve the agreement between computations and observations of irradiance variations at various wavelengths.

The properties of a single-component solar atmosphere model, such as model C, show us the basic properties of spectrum, but this is an oversimplification because of the surface structures on the solar disk having different distributions of temperature and density with height. Therefore, much or all of the variability in the Sun's output appears to arise from the variation in the contributions from the different structures over the solar cycle. When we integrate the continuum spectra (computed without including line opacities or emissivities), using area weights as in Table 5, we obtain a first estimate of the total solar irradiance of ~ 1600 W m^{-2}. These values are $\sim 18\%$ larger than the observed values of ~ 1368 W m^{-2} because the lines were not included.

Solanki & Unruh (1997) recently made estimates of solar spectral irradiance variations. These authors show that neither the Planck spectrum with a varying $T_{\rm eff}$ nor two-component models containing quiet Sun and faculae can explain the solar irradiance variability compiled by Lean (1991). Also, these authors conclude that the effects of sunspots cannot be neglected because, even when the area of the disk covered by sunspots is small, their contrast is rather large. These authors use a simple approach based on height of formation, which does not take into account detailed solution of the radiative transfer equations for many lines with their departures from LTE (see Appendix A). Also, these authors refer to the models FAL-C, FAL-F, and FAL-P, which must not be confused with our current models. The models used by these authors are versions of earlier models that do not have the crossover of the $T(z)$ curves in the deep photosphere of our models (see Fig. 7*a*) and, therefore, cannot explain the reversal of the plage contrast at 1.6 μm. Also, the large variations in opacity due to lines make the assignment of a "height of formation" uncertain for wide spectral bands containing many lines that form in various regions far from the neighboring continuum.

In spite of the differences, our preliminary results qualitatively agree with Solanki and Unruh findings, and in particular we agree in that the changes of the solar spectral irradiance can be fully explained by the magnetic structures on the solar disk. This is especially true in the UV, where the large variations are explained by changes in the chromosphere and transition region closely correlated to the presence of strong magnetic fields. Even in photospheric and low chromospheric layers, the substantial variations in the lines and continuum in plage may account for the changes in the visible irradiance spectrum. However, at present we cannot rule out some global variations in the photospheric layers due to changes in the convection that may cause slight variations in the continuum that have not yet been measured. It may be possible that such changes decrease the radiation from nonmagnetic areas of the Sun, thus compensating for some of the increases in active regions.

We are completing calculations of the 3920–4120 Å, 4900–5100 Å, and 8520–8720 Å bands currently being measured with the Variability of Irradiance and Gravity Oscillations (VIRGO) instrument on board *SOHO* (Frohlich et al. 1995). Calculations of the bands at 4080–4120 Å and 6050–6100 Å for the SunRISE precision solar photometric telescope (PSPT; J. Kuhn 1997, private communication) are finished and will be studied in the following papers. We believe that the combination of these and other observations, together with analysis based on the methods we describe here and Paper II, will advance our understanding of the origin of spectral irradiance variations.

J. F. acknowledges partial support from NSF through the RISE program grant, NCAR proposal 1997-014, Application of Spectra Synthesis to the Study of Solar Visible, UV, EUV, and Infrared Variability. This work was also supported by the *UARS* SOLSTICE Project (Gary Rottman, Principal Investigator) under NASA grant 5-5050. We thank Roberto Casini for his careful reading of the manuscript and his constructive suggestions, which improved the paper. We also thank the referee for numerous suggestions, which improved the manuscript.

APPENDIX A

APPROXIMATE LINE SOURCE FUNCTION

The new method we describe here permits estimates of the source function for any line and is derived from the two-level atom approximation. The method estimates the population ratio of two levels experiencing radiative and collisional transitions but does not estimate the absolute populations. Thus, the transition lower level population is supposed to be known as function of height (for instance in LTE). This procedure is adequate for resonance lines (where the lower level population is close to the total species density), or when the lower level is close to the continuum (and can be assumed to follow the Boltzman law with respect to the known continuum population) but will not be accurate in the cases of transitions whose lower levels have intermediate excitation energies.

Let us consider a single line emission and absorption superimposed on a continuum due to other species, for instance hydrogen and metals continuum emission and absorption. We also include in this "continuum" any other opacities and emissions that are known (e.g., H lines resulting from a full non-LTE computation).

In the two-level approximation, the line source function at any level of the atmosphere can be expressed by

$$S_{\rm lin} = \frac{\bar{J} + \xi B}{1 + \xi} , \tag{A1}$$

where $\bar{J}$ is the angular mean intensity averaged throughout the line profile (see below), ξ is the ratio of collisional to radiative deexcitation, and B is the Planck function. This formula results from considering the atomic level populations and transition rates. The formula can be modified for taking onto account other transitions, but we omit this here for simplicity.

The mean intensity results from the integral

$$\bar{J} = \int_\nu \Phi_\nu J_\nu \, d\nu , \tag{A2}$$

where Φ_ν is the absorption line profile normalized to an integrated value of unity and J_ν is the monochromatic angular mean intensity.

The main problem in equation (A1) is that it requires knowledge of J, which in turn depends on the line source function (and on the continuum source function) through the radiative transfer equation. Our scheme includes a simple analytical approximation for such dependence. Then, we eliminate all unknowns but one, and we obtain an equation that permits obtaining that unknown, the line source function, in terms of known quantities.

To obtain J_ν we need to solve the radiative transfer equation considering all opacity and emissivity sources. It is customary to express the total source function as

$$S_\nu = \frac{\varphi_\nu S_{\rm lin} + r_\nu S_{\rm cont}}{\varphi_\nu + r_\nu} , \tag{A3}$$

where r_ν is the ratio of the continuum to the line opacity at line center, J_ν is the line profile normalized to unity at line center (note that this profile is normalized differently from Φ_ν), and $S_{\rm cont}$ is the continuum source function. This equation can be modified to account for PRD; however, here we omit these developments for simplicity.

Equation (A3) gives the total source function in terms of known parameters and the line source function $S_{\rm lin}$. The angle averaged radiation intensity at one level of the atmosphere involves integration over all heights, and can be expressed by the equation

$$J_\nu = \Lambda_\nu S_\nu , \tag{A4}$$

where Λ_ν is the formal integration operator that is described in the literature (e.g., see Fontenla & Rovira 1985b). Replacing the total source function from equation (A3) we obtain

$$J_\nu = \Lambda_\nu\left(\frac{\varphi_\nu S_{\rm lin}}{\varphi_\nu + r_\nu}\right) + \Lambda_\nu\left(\frac{r_\nu S_{\rm cont}}{\varphi_\nu + r_\nu}\right) . \tag{A5}$$

Now we evaluate the angle-averaged intensity in equation (A2), and we obtain the following detailed expression for the mean intensity:

$$\bar{J} = \int_\nu \Phi_\nu\left[\Lambda_\nu\left(\frac{\varphi_\nu S_{\rm lin}}{\varphi_\nu + r_\nu}\right) + \Lambda_\nu\left(\frac{r_\nu S_{\rm cont}}{\varphi_\nu + r_\nu}\right)\right] d\nu , \tag{A6}$$

where the mean intensity is expressed in terms of the line source function and known parameters through two integrals, one in frequency, and another in height (this one represented by the operator Λ.

To simplify the results, we choose to first modify equation (A1) to the equivalent form that follows:

$$(1 + \xi) S_{\rm lin} = \bar{J} + \xi B . \tag{A7}$$

Here we substitute the mean intensity from equation (A6) and obtain

$$(1 + \xi) S_{\rm lin} = \int_\nu \Phi_\nu \Lambda_\nu\left(\frac{\varphi_\nu S_{\rm lin}}{\varphi_\nu + r_\nu}\right) d\nu + \int_\nu \Phi_\nu \Lambda_\nu\left(\frac{r_\nu S_{\rm cont}}{\varphi_\nu + r_\nu}\right) d\nu + \xi B , \tag{A8}$$

where we also separated the frequency integral in two terms.

Equation (A8) is basically the result we want because it has only one unknown, the line source function, together with several known parameters and operators. These known parameters include the line and continuum opacity, both in r_ν and implicitly in the operator Λ. The line opacity does not depend directly on the population ratios, but only on the lower level population, except for the usually small stimulated-radiation term. However, in general the lower level population depends on the full non-LTE statistical equilibrium that may have dependency on the line source function as well. Here we neglect such dependency and assume the lower level population as a given parameter. Equation (A8) can be solved for the values of the line source function, $S_{\rm lin}$ (as function of height).

Moving to the left-hand side of the equation all terms that contain the line source function, we obtain

$$(1+\xi)S_{\rm lin} - \int_\nu \Phi_\nu \Lambda_\nu \left(\frac{\varphi_\nu S_{\rm lin}}{\varphi_\nu + r_\nu}\right) d\nu = \int_\nu \Phi_\nu \Lambda_\nu \left(\frac{r_\nu S_{\rm cont}}{\varphi_\nu + r_\nu}\right) d\nu + \xi B \ . \tag{A9}$$

Although in principle simple, equation (A9) is complicated by the integrals involved. This equation could be fully solved by expressing numerically these integrals in a matrix operator form and then inverting the resulting left side matrix operator. This procedure is accurate but cumbersome for the many lines and heights that need to be included in our calculation. Thus, we consider a simpler but approximate expression of the line source function.

To represent the result of the height and frequency integrals it is customary to define the line net radiative bracket, ρ. However several variations of the definition this parameter have been used in the literature. One of them considers the line source function (see Fontenla & Rovira 1985a) and can be modified by considering the continuum opacity. Following this we define ρ as the quantity that satisfies the following equation:

$$\int_\nu \Phi_\nu \Lambda_\nu \left(\frac{\varphi_\nu S_{\rm lin}}{\varphi_\nu + r_\nu}\right) d\nu = (1-\rho) \int_\nu \Phi_\nu \left(\frac{\varphi_\nu S_{\rm lin}}{\varphi_\nu + r_\nu}\right) d\nu \ , \tag{A10}$$

where the parameter ρ is a dimensionless number. Thus, the value of ρ at each height depends on the whole atmosphere and is a frequency-averaged value.

In the equations shown here we have assumed that $S_{\rm lin}$ is frequency independent; however, it is easy to show that a similar formula with additional terms can be derived for frequency-dependent cases where coherent scattering in the line is included in equation (A1).

Using this definition in equation (A9), we obtain the final expression for the line source function:

$$S_{\rm lin} = (\xi + R_{\rm cont} + \rho R_{\rm lin})^{-1} \left[\int_\nu \Phi_\nu \Lambda_\nu \left(\frac{r_\nu S_{\rm cont}}{\varphi_\nu + r_\nu}\right) d\nu + \xi B \right] , \tag{A11}$$

where the R terms are given by

$$R_{\rm cont} = 1 - \int_\nu \Phi_\nu \left(\frac{\varphi_\nu}{\varphi_\nu + r_\nu}\right) d\nu = \int_\nu \Phi_\nu \left(\frac{r_\nu}{\varphi_\nu + r_\nu}\right) d\nu \ ,$$

$$R_{\rm lin} = \int_\nu \Phi_\nu \left(\frac{\varphi_\nu}{\varphi_\nu + r_\nu}\right) d\nu = 1 - R_{\rm cont} \ . \tag{A12}$$

Considering equation (A10), one finds that for optically thin lines the integral term in the left-hand side is negligible compared with the line source function (regardless of the value of ρ). Consequently, in the optically thin limit when ρ is close to unity, a good approximation is

$$\rho \approx 1 - \tau_{\rm lin} \ ,$$

where τ is the optical depth at a frequency representative of the line core.

When the line is optically thick, the integral term approaches the line source function and ρ approaches zero. However, Fontenla & Rovira (1985b) show that at large optical depths any local expression becomes incorrect as the diffusion limit is reached. In this limit the difference between J and S turns into the second derivative of S with respect to τ. In intermediate cases ρ may have a very complicated behavior and may even become small and negative when "backwarming" is significant (see, e.g., FAL1).

In most cases a reasonable approximation for the net radiative bracket is

$$\rho \approx Ei_2(\tau_{\rm lin}) \ , \tag{A13}$$

where Ei_2 is the second integral exponential function. This formula is exact only for constant source function. However, it gives a reasonable approximation in optically thin cases and in all cases when the source function varies slowly with height. These are the cases of the transition region lines and the optically thick lines formed in the chromosphere, respectively. In the case of photospheric lines, the use of the actual value of ρ is not very important because the e term dominates and the source function becomes close to the Planck function. This occurs in all cases at photospheric layers just below $z = 0$ (viz., $\tau_{5000} = 1$).

The integral in the right-hand side of equation (A13) can be computed by approximating the line profile with a Gaussian function. We found that a reasonable approximation (with error $< 20\%$) to this integral truncated at 1 Doppler width is given

by the following formula:

$$\rho = \frac{1.7 + 2.8\tau^2 + 0.07\tau^3}{2 + 16\tau^2 + 6\tau^3 + \tau} . \tag{A14}$$

Using the approximation of equation (A14), one can estimate the line source function in equation (A11), without solving ρ in full detail.

Note that equation (A11) approaches the optically thin usual approximation for very small τ, and, when the continuum term is neglected,

$$\tau_{\rm lin} \ll 1 \Rightarrow \rho \approx 1 ,$$
$$S_{\rm lin} \approx (\xi + 1)^{-1}\xi B .$$

Also, note that, for the chromospheric optically thick lines, when the continuum is neglected we obtain

$$\tau_{\rm lin} \cong 1 \Rightarrow \rho \approx Ei_2(\tau_{\rm lin}) ,$$
$$S_{\rm lin} \approx (\xi + 1)^{-1}\xi B ,$$

which differs substantially from the optically thin approach. This difference arises from the fact that, for the regions responsible of the line core, the value of ξ is very small in all cases (because of the small electron density) but, also, ρ is much smaller than unity because of the large optical thickness. Thus, in this case the value of ξ must not be compared with unity but rather with the small value of ρ. Consequently, the source function for the optically thick chromospheric lines does not drop with decreasing density layers as much as it would drop in an optically thin case. This effect occurs entirely because of the emitted photon reabsorption and reemission and is a radiative transfer effect.

Using equations (A11) and (A14), it is possible to obtain reasonable estimates of line self-reversal and emission cores, in all cases regardless of optically thin or thick conditions. However, considering more accurate collisional deexcitation, and including multilevel atom corrections can improve our scheme results.

Note that our formulas are somewhat similar to those used by other authors, e.g. Anderson (1989) and Anderson & Athay (1989). However, there are a few differences, and the most important difference is that we consider the effects of continuum radiation in increasing the atom excitation and the line source function. These effects come through the coefficients R in the denominator and the term with $S_{\rm cont}$ in the numerator of equation (A11). These terms produce some differences close to the temperature minimum and thus affect the central core of low chromospheric lines. We call this term as the "continuum contribution to the line source function," and it results from the radiative excitation due to the illumination by continuum radiation.

In some cases the continuum terms are important, and such is the case of the triplet lines of He. Full non-LTE calculations of the source function of the He 10,830 Å line yield about $\frac{1}{2}$ the value of the incident continuum radiation (see Avrett et al. 1994). This line, although optically thin in most of the solar atmosphere (and marginally thick in prominences and active regions), is formed in the chromosphere with $\epsilon \ll 1$. However, this line source function is not as small as a simple two-level atom model without our continuum terms would predict. The dominant term for the line excitation arises from the illumination by photospheric layers where $\tau \sim 1$, and the radiation is diluted to about $\frac{1}{2}$ because the layers where the line forms are irradiated only from one side. This case is explained in detail to show how a simple-minded optically thin estimate may yield very inaccurate results.

A reasonable approximation for the continuum contribution can be obtained from the equation

$$\int_\nu \Phi_\nu \Lambda_\nu \left(\frac{r_\nu S_{\rm cont}}{\varphi_\nu + r_\nu}\right) d\nu \sim S_0\, Ei_2(\tau - \tau_0) \int_\nu \Phi_\nu \left(\frac{r_\nu}{\varphi_\nu + r_\nu}\right) d\nu = S_0\, Ei_2(\tau - \tau_0) R_{\rm cont} , \tag{A15}$$

where S_0 and τ_0 are the continuum source function and total optical depth at the layer where the local continuum intensity forms.

APPENDIX B

RELATIONSHIP BETWEEN DISK INTENSITY AND IRRADIANCE

The emergent intensity from a stellar surface is the limiting case of the outward specific intensity at the boundary of a star. When all the parameters of the solar atmosphere (temperature, density, atomic composition, etc.) vary only in the radial direction, the emergent intensity at any point of the solar surface depends only on the angle between the local normal to the solar surface and the line of sight. The value of the intensity is the same all along the line of sight toward the Earth. We define the "average disk intensity" at any particular wavelength and time as the sum over the entire solar disk of the emergent intensities in the direction toward the Earth, weighted by the apparent emitting area, divided by the total solar disk area.

Note that while both intensity and flux are defined as energy per unit time per unit area, the two are fundamentally different. For the intensity, one identifies the direction of the radiation and the area of the emitting surface, while for the flux we integrate over all directions of the radiation field for a particular orientation of an irradiated surface. The flux or irradiance on a surface outside the Sun is computed by integrating the contributions from the entire solar disk. This integral is, thus, dependent on the orientation of the collecting surface because the projected area of this surface may vary from unity to zero as

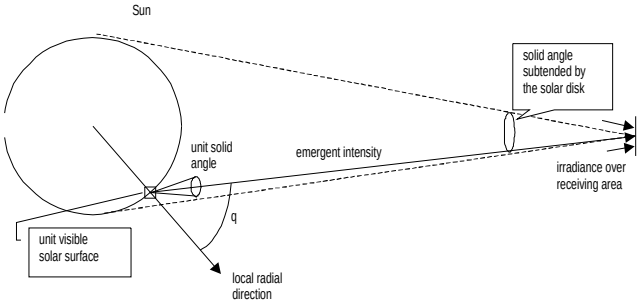

FIG. 8.—Schematic describing the relationship between solar irradiance at the Earth and intensity emergent from the Sun in the direction of the Earth. The average disk intensity is the emergent intensity averaged over the entire solar disk.

the collecting area rotates from normal incidence to zero. The irradiance at the Earth is a particular case of the radiation flux; viz., it is the flux at 1 AU through a surface normal to the Sun-Earth line. The relationship between the disk intensity and the spectral irradiance is shown in Figure 8.

The average disk intensity, I_a, times the area of the solar disk, A_s, gives the total amount of radiation that the Sun emits toward the unit area collecting surface, A_c. Thus, the radiative flux R (that is, the radiative energy per unit area and unit wavelength) that crosses the collecting surface is

$$R = \left[I_a A_s \left(\frac{A_c}{D^2} \right) \right] \frac{1}{A_c} , \tag{B1}$$

where D is 1 AU and (A_c/D^2) is the solid angle subtended by the collecting area. Since the collecting area appears in the denominator and numerator, it cancels to give the simple relation between irradiance and the average solar disk intensity. The irradiance is then

$$R = I_a \left(\frac{A_s}{D^2} \right) = \Omega I_a , \tag{B2}$$

where Ω is the angle subtended by the solar disk from 1 AU. This simple expression relates the average disk intensity at the surface of the Sun to the incident flux on the terrestrial atmosphere. This formula can be expressed in units commonly used for irradiance as

$$R(\mathrm{W\ m^{-2}\ nm^{-1}}) = \frac{\Omega}{100} I_a(\mathrm{ergs\ s^{-1}\ cm^{-2}\ sr^{-1}\ \AA^{-1}}) . \tag{B3}$$

Another useful quantity is the solar disk brightness temperature, T_{bri}, which is the temperature that entered in the Planck function gives the average disk intensity at a given wavelength. T_{bri} is computed as

$$T_{\mathrm{bri}} = \frac{hv}{k} \ln^{-1} \left(\frac{2hv^4}{c^2 \lambda} \frac{1}{I_a} + 1 \right) , \tag{B4}$$

where h and k are the Planck and Boltzmann constants, c is the speed of light, and v and λ are the radiation frequency and wavelength. The numerical constants are $h/k = 4.79943 \times 10^{-11}$ s K, and $2h/c^2 = 1.4743 \times 10^{-47}$ ergs s^3 cm^{-2} sr^{-1}.

REFERENCES

Aller, L. H. 1963, The Atmospheres of the Sun and Stars (New York: Ronald), 192
Anderson, L. S. 1989, ApJ, 339, 558
Anderson, L. S., & Athay, R. G. 1989, ApJ, 346, 1010
Athay, R. G. 1976, The Solar Chromosphere and Corona: The Quiet Sun (Boston: Reidel)
Avrett, E. H. 1985, in Chromospheric Diagnostics and Modeling, ed. B. W. Lites (Sunspot, NM: National Solar Observatory), 67
———. 1990, in Solar Photosphere: Structure, Convection, and Magnetic Fields, ed. J. O. Stenflo (Dordrecht: Kluwer), 3
———. 1995, in Infrared Tools for Solar Astrophysics: What's Next?, ed. J. Kuhn & M. Penn (Singapore: World Scientific), 303
———. 1998, in Solar Electromagnetic Radiation Study for Solar Cycle 22, ed. J. M. Pap, C. Frohlich, & R. K. Ulrich (Dordrecht: Kluwer), 449
Avrett, E. H., Fontenla, J. M., & Loeser, R. 1994, in Infrared Solar Physics, ed. D. M. Rabin, J. T. Jefferies, & C. Lindsey (Dordrecht: Kluwer), 35
Avrett, E. H., & Loeser, R. 1992, in ASP Conf. Ser. 26, 7th Cambridge Workshop on Cool Stars, Stellar Systems, and the Sun, ed. M. S. Giampapa & J. A. Bookbinder (San Francisco: ASP), 489
Ayres, T. R. 1995, in Infrared Tools for Solar Astrophysics: What's Next?, ed. J. Kuhn & M. Penn (Singapore: World Scientific), 289
Ayres, T. R., & Wiedemann, G. R. 1989, ApJ, 338, 1033
Bohm, K.-H. 1960, in Stellar Atmospheres, ed. J. L. Greenstein (Chicago: Univ. of Chicago Press), 88
Brown, S. A., Folk, M., Goucher, G., & Rew, R. 1993, Comput. Phys., 7, 304
Collados, M., Pillet, V. M., Cobo, B. R., Del Toro Iniesta, J. C., & Vazquez, M. 1994, A&A., 291, 622
Cox, D. P., & Tucker, W. H. 1969, ApJ, 157, 1157
Delbouille, L., Roland, G., Brault, J., & Testerman, L. 1981, Photometric Atlas of the Solar Spectrum from 1850 to 10,000 cm^{-1} (Tucson: KPNO)
Floyd, L., Reiser, P., Crane, P., Herring, L., & Brueckner, G. 1998, Sol. Phys., 177, 105
Fontenla, J. M. 1994, in Proc. Third *SOHO* Workshop on Solar Dynamic Phenomena and Solar Wind Consequences ESA SP-373, ed. J. J. Hunt (Noordwijk: ESA), 47
Fontenla, J. M., & Avrett, E. H. 1993, in Proc. First *SOHO* Workshop on Coronal Streamers, Coronal Loops, and Coronal and Solar Wind Composition, ESA SP-348, ed. C. Mattok (Noordwijk: ESA), 335
Fontenla, J. M., Avrett, E. H., & Loeser, R. 1989, ApJ, 355, 700 (FAL1)
———. 1992, ApJ, 377, 712 (FAL2)
———. 1993, ApJ, 406, 319 (FAL3)
Fontenla, J. M., Reichmann, E. J., & Tandberg-Hanssen, E. 1988, ApJ, 329, 464

Fontenla, J. M., & Rovira, M. 1985a, Sol. Phys., 96, 53
———. 1985b, J. Quant. Spectrosc. Radiat. Transfer, 34, 389
Fontenla, J. M., Tandberg-Hanssen, E., Reichmann, E. J., & Filipowski, S. 1989, ApJ, 344, 1034
Foukal, P., Little, R., Graves, J., Rabin, D., & Lynch, D. 1990, ApJ, 353, 712
Fox, P., Fontenla, J. M., White, O. R., Harvey K., & Avrett, E. 1999, in preparation (Paper II)
Fraunhofer, J. 1817, Denkschr. Konig, Akad. Wiss., 5, 193
Frohlich, C., et al. 1995, Sol. Phys., 162, 101
Gingerich, O., Noyes, R. W., Kalkofen, W., & Cuny, Y. 1971, Sol. Phys., 18,347
Gurman, J. B. 1984, Sol. Phys., 90, 13
Harvey, K. L., & White, O. R. 1999, ApJ, 515, 814
Hickey, J. R., Alton, B. M., Kyle, H. L., & Hoyt, D. 1988, Space Sci. Rev., 48, 321
Hinteregger, H. E. 1976, J. Atmos. Terr. Phys., 38, 791
Hinterreger, H. E., Fukui, K., & Gibson, B. R. 1981, Geophys. Res. Lett., 8, 1147
Holweger, H. 1967, Z. Astrophys., 65, 365
Holweger, H., & Muller, E. A. 1974, Sol. Phys., 39, 19
Kiepenheuer, K. O. 1953, in The Sun, ed. G. Kuiper (Chicago: Univ. of Chicago Press), 322
Kurucz, R. L. 1992a, Rev. Mexicana Astron. Astrofis., 23, 45
———. 1992b, Rev. Mexicana Astron. Astrofis., 23, 181
———. 1992c, Rev. Mexicana Astron. Astrofis., 23, 187
———. 1995, in ASP Conf. Ser. 81, Laboratory and Astronomical High-Resolution Spectra, ed. A. J. Sauval, R. Blomme, & N. Grevesse (San Francisco: ASP), 583
Kurucz, R. L., & Avrett, E. H. 1981, Solar Spectrum Synthesis. I. A Sample Atlas from 224 to 300 nm, SAO Spec. Rept. 391 (Cambridge: SAO)
Kurucz, R. L., & Bell, B. 1995, CD-ROM 23 (Cambridge: SAO)
Kurucz, R. L., & Furenlid, I. 1980, A Sample Spectral Atlas for Sirius, SAO Spec. Rept. 387 (Cambridge: SAO)
Lean, J. 1991, Rev. Geophys., 29, 505
Lemaire, P., Gouttebroze, P., Vial, J. C., & Artzner, G. E. 1981, A&A, 103, 160
Lites, B. W., & Skumanich, A. 1992, ApJS, 49, 293
Maltby, P., Avrett, E. H., Carlsson, M., Kjeldseth-Moe, O., Kurucz, R. L., & Loeser, R. 1986, ApJ, 306, 284
Mihalas, D. 1978, Stellar Atmospheres (San Francisco: Freeman)
Neckel, H., & Labs, D. 1984, Sol. Phys., 90, 205
Porter, J. G., Fontenla, J. M., & Simnett, G. 1995, ApJ, 438, 472
Rew, R. K., & Davis, G. P. 1990, IEEE Comput. Graphics App., 10, 76
Rew, R. K., Davis, G. P., Emmerson, S., & Davies, H. 1997, NetCDF User's Guide for C, An Interface for Data Access, Version 3 (Boulder: Unidata [UCAR])
Rottman, G. J., Woods, T. N., & Sparn, T. N. 1993, J. Geophys. Res., 97(10), 119
Shine, R. A., & Linsky, J. L. 1974, Sol. Phys., 39, 49
Solanki, S. K., & Unruh, Y. C. 1997, A&A, 18,4
Spitzer, L. 1962, The Physics of Fully Ionized Gases (New York: Interscience)
Tobiska, W. K. 1992, in Proc. Workshop on the Solar Electromagnetic Radiation Study for Solar Cycle 22, ed. R. F. Donnelly (Springfield, VA: Natl. Tech. Info. Serv.)
Topka, K. P., Tarbell, T. D., & Title, A. M. 1992, ApJ, 396, 351
———. 1997, ApJ, 484, 479
Uitenbroek, H., Noyes, R. W., & Rabin, D. 1994, ApJ, 432, L67
Vernazza, J. E., Avrett, E. H., & Loeser, R. 1981, ApJS, 45, 635 (VAL)
Vernazza, J. E., & Reeves, E. M. 1978, ApJS, 37, 485
Wang, H., Spirock, T., Goode, P. R., Lee, C., Zirin, H., & Kosonocky, W. 1998, ApJ, 495, 957
White, O. R., De Toma, G., Rottman, G., Woods, T. N., & Knapp, B. G. 1998, Sol. Phys., 177, 89
Willson, R. C. 1982, J. Geophys. Res., 87, 4319
Willson, R. C., & Hudson, H. S. 1991, Nature, 351, 42
Wollaston, W. H. 1802, Philos. Trans. I, 365